12-2023

Maximum Depositional Age Analysis using Paired LA-ICP-MS and CA-ID-TIMS Detrital Zircon U-Pb Geochronology

Benjamin L. Howard
University of Arkansas, Fayetteville

Maximum Depositional Age Analysis using Paired LA-ICP-MS and CA-ID-TIMS Detrital Zircon U-Pb Geochronology

A thesis submitted in partial fulfillment
of the requirements for the degree of
Master of Science in Geology

by

Benjamin L. Howard
University of Iowa
Bachelor of Science in Geoscience, 2021

December 2023
University of Arkansas

This thesis is approved for recommendation to the Graduate Council.

_____
Glenn Sharman, Ph.D.
Thesis Director

_____
Celina Suarez, Ph.D.
Committee Member

_____
Gregory Dumond, Ph.D.
Committee Member

Abstract

The "law of detrital zircons" states that a sedimentary unit cannot be older than its youngest detrital zircon. The youngest U-Pb date(s) from detrital zircon may thus be used to infer a given sedimentary deposit's maximum depositional age (MDA). MDAs may be calculated in various ways using dates from zircon U-Pb geochronology. Common dating methods used for U-Pb geochronology are laser ablation-inductively coupled plasma-mass spectrometry (LA-ICP-MS) and chemical abrasion-isotope dilution-thermal ionization mass spectrometry (CA-ID-TIMS), a low- and high-resolution instrument type, respectively. Chapter 2 will systematically compare paired LA-ICP-MS and CA-ID-TIMS dates from the same zircon grains to assess the agreement between these two methods. Previous case studies have noted that U-Pb dates acquired via both dating methods from the same zircon crystals are often different and can result in MDA calculations that are not within uncertainty of one another. This work is motivated by the growing number of MDA and detrital zircon studies since the 1980s. Chapter 3 will consist of a case study where paired LA-ICP-MS and CA-ID-TIMS dates are applied to the Elliot Formation of South Africa with the goal of better constraining the stratigraphic placement of the end-Triassic mass-extinction (ETE) and Triassic-Jurassic boundary (TJB).

In Chapter 2, I investigate the degree of agreement between zircon U-Pb dates analyzed via LA-ICP-MS and CA-ID-TIMS by compiling data from published literature. I compiled a database of 49 publications with 1528 paired LA-ICP-MS and CA-ID-TIMS analyses from 16 laboratories. The database shows LA-ICP-MS $^{206}Pb/^{238}U$ dates to be systematically younger than the corresponding CA-ID-TIMS dates, with the mode of the age offset distribution shifted by ~2-2.5%. This shift hints at the possibility of "matrix effects", Pb loss, and/or inheritance.

Chapter 3 focuses on the Elliot Formation in South Africa, a paleontologically significant Triassic-Jurassic fluvial system. Unlike the overlying Clarens Formation, the upper section of the Elliot Formation is taxonomically diverse. The lower section of the Elliot Formation is poorly sampled and appears to be less diverse than the upper section. The precise age of the Elliot Formation, including the stratigraphic placement of the ETE, TJB, and Central Atlantic Magmatic Province (CAMP) is poorly constrained. This research will focus on the type section, Barkley Pass, of the Elliot Formation. A detrital zircon study of the Elliot Formation at Barkley Pass, the first of its kind at this locality, would constrain the stratigraphic position of the ETE and the TJB and place paleontological studies into a new chronologic framework. I present analysis of 18 detrital zircon samples from the Elliot Formation at Barkley Pass. I was able to constrain the MDA of the Elliot Formation to 208.80 ± 0.14 Ma near the base of the section and 194.65 ± 0.13 Ma near the top. I have found that the uppermost Lower Elliot Formation is Early Jurassic in age and not Late Triassic as previously thought, which is supported by preliminary C-isotope data placing the onset of the ETE to 154 m from the base of the Elliot Formation.

Acknowledgements

To all that read this document, let it be known that I did not write it. I am a product of many hands that have molded and come together over space and time to this moment and any moment in my life hereafter. This document should not be entitled as “written by Benjamin L. Howard”, but instead “written by Giants”.

Some of these mentioned giants are those everyone knows. Names like John D. Rockefeller, Jordan Peterson, even Marlon Brando. All the giants in my life fostered this document by one steppingstone or another. But giants do not have to be all too well known to be the reason for my thesis. Giants, like most things, come in all shapes and sizes. I will do the best I can to name a few of the giants in my life, but there will inevitably be one name not mentioned that is deserved to, and for that, I apologize.

I give my thanks to the many authors cited in this work, for your support and collaboration; to Glenn Sharman, Celina Suarez, and Gregory Dumond for professional guidance; to Joe Bauman, for the philosophy of an oil hunter; to Mac McGilvery, Steve Milligan, and Chris Liner, for career development; to Jack Fekete and Quinten Jones, for camaraderie and unending support through graduate school; to Brad Cramer and Kate Tierney for showing me the wonderful world of geology and all the mysteries it holds; and to the tallest of them all, Emily Finzel, for taking a bet on a stupid kid, and making everything he ever wanted possible, and within grasp.

I also acknowledge the boys back home, for getting me out of small-town USA and making me miss it every day. I extend my gratitude to Abby and Racheal, for teaching me how to grow up and be the brother I should be, to Mom for always being there and loving us through it all, and to Dad, for pushing me, for molding me, for being the best damn man you could ask for, and for getting it right.

To Lidija, my star at night, my sun in the day, moja ljubav zauvek. All I have, for you.

“If I have seen further, it is by standing on the shoulders of giants.” -Sir Isaac Newton

Table of Contents

List of Figures

Chapter 1: Introduction

Detrital zircon dating has been widely used to constrain the timing of large-scale geologic events and the maximum depositional age (MDA) of sedimentary deposits (Gehrels, 2014; Sharman and Malkowski, 2020). MDA studies have become much more common over the last 20 years (Fig. 2.1) and are likely to continue along this trend. Common dating methods used for MDA studies are LA-ICP-MS and CA-ID-TIMS. Chemical abrasion, a common laboratory practice used in CA-ID-TIMS analyses, uses HF acid to remove metamict zones from a zircon. Metamict zones in zircon are corrupted from high amounts of radiation damage and can facilitate Pb loss. Pb loss is the removal of Pb (the daughter product from the U-Pb radioactive decay system) from a zircon, which, when analyzed, makes a grain appear too young. Because it is not common practice to chemically abrade zircon before LA-ICP-MS, it is possible that U-Pb dates acquired via LA-ICP-MS could be younger than if the same analysis were conducted by higher resolution CA-ID-TIMS and if Pb loss was present.

It is imperative to understand any possible discrepancy that non-CA treated LA-ICP-MS U-Pb dates have due to the incorporation of zones that have undergone Pb loss and how those resulting dates affect MDA calculations. There has yet to be a large-scale compilation of paired non-CA LA-ICP-MS and CA-ID-TIMS analyses from the same zircon grains. Such a comparative dataset would help characterize the degree of agreement between the two instrumentation methods and assess the role that unmitigated Pb loss or other factors may play in causing U-Pb dates acquired via non-CA LA-ICP-MS to be too young.

A case study to test the insights from my comparative analysis on new, geologically significant, real-world data is necessary to ensure theoretical findings have experimental grounding. The Elliot Formation in South Africa fits these criteria based on its significant time of

deposition (before, during, and after the ETE, TJB, and CAMP volcanism) and its highly fossiliferous nature. I have collected both non-CA LA-ICP-MS data from randomly selected grains and paired non-CA LA-ICP-MS and CA-ID-TIMS data from handpicked grains from the same samples. With this case study I can compare MDAs derived from LA-ICP-MS data (both random and handpicked) with higher resolution CA-ID-TIMS results.

Chapter 2: Tandem LA-ICP-MS and CA-ID-TIMS Detrital Zircon U-Pb Geochronology: Analysis of a Global Dataset

Introduction

Zircon U-Pb geochronology is a commonly used dating technique that is applied to igneous, metamorphic, and sedimentary systems (Gaschnig et al., 2010; Gehrels, 2014; Finzel and Rosenblume, 2021; Olierook et al., 2021). The zircon U-Pb radiometric system is a highly effective geochronometer due to its ability to survive multiple sedimentary cycles and be utilized in a diverse range of geologic settings. Thus, zircon has been widely used in geochronologic studies for over 70 years (Davis et al., 2003; Dröllner et al., 2022). The past 30 years have seen a rapid increase in publications relating to detrital zircon geochronology per year, and this trend is likely due primarily to the growth in *in-situ* analysis via LA-ICP-MS (Fig. 2.1) (Coutts et al., 2019; Gehrels et al., 2020; Sharman and Malkowski, 2020).

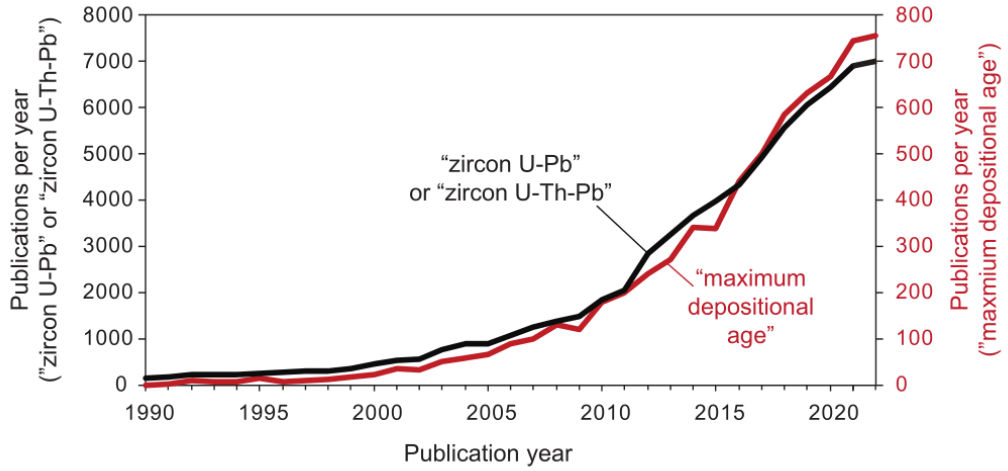

Figure 2.1: The number of publications per year containing the phrases "zircon U-Pb" or "zircon U-Th-Pb" and "maximum depositional age"; data from Google Scholar search results (after Coutts et al., 2019 and Sharman and Malkowski, 2020).

Three types of mass spectrometers that are commonly used for U-Pb analysis in zircon are: 1. secondary ionization mass spectrometry (SIMS), 2. laser ablation-inductively coupled plasma-mass spectrometry (LA-ICP-MS), and 3. chemical abrasion-isotope dilution-thermal ionization mass spectrometry (CA-ID-TIMS). The choice of mass spectrometer type often depends on the study in question. LA-ICP-MS is very cost effective ($2-8/analysis) and time efficient and is often used for studies looking at bulk age distributions, such as for provenance analysis (Gehrels et al., 2020; Gardner et al., 2022). CA-ID-TIMS is often used for situations where high-precision data is necessary, like MDA studies (Keeley et al., 2012; Cox et al., 2018; Herriot et al., 2019).

"Matrix effects" related to laser-induced element fractionation are biases that refers to the impact of differences in zircon matrix properties between standards and unknowns on the accuracy and precision of dating with LA-ICP-MS (Black, 1987; Murakami et al., 1991; Allen and Campbell, 2012). Matrix effects are controlled by the amount of alpha decay radiation damage a zircon has experienced with the less radiation damage, the more disproportionately young a zircon appears (Sliwinski et al., 2017). Inheritance is the incorporation of older zircon cores in an analysis. Because CA-ID-TIMS analyses use a whole zircon grain, older cores can make a zircon with secondary growth rims appear older (Gehrels, 2014). Pb loss is promoted by incorporating high amounts of U and Th which leads to metamictization, fracturing of the zircon grain, and then removal of Pb, often through hydrothermal processes (Cherniak and Watson, 2000; Zi et al., 2022). Removing radiogenic Pb makes the zircon date appear to be too young (Geherals, 2014). Pb loss in zircon can be mitigated prior to analysis using two practices: (1) thermal annealing at 900ºC to repair and recrystallize metamict zones, melt multi-phase inclusions, and homogenize grains; and (2) chemical abrasion with HF acid at 220ºC to dissolve and remove damaged parts of the zircon that are more likely to have undergone Pb loss (Ginster et al., 2003; Morales et al., 2022; McKanna

et al., 2023). Although this treatment is common practice prior to analysis via ID-TIMS, zircon analyzed via LA-ICP-MS are irregularly treated with thermal annealing and rarely with chemical abrasion, suggesting that these data have a greater potential to have been influenced by Pb loss (Widmann et al., 2019).

Common isotopic ratios used to calculate radiometric dates in zircons are as follows: $^{206}Pb/^{238}U$, $^{207}Pb/^{235}U$, and $^{207}Pb/^{206}Pb$. Studies often use either the $^{206}Pb/^{238}U$ date when interpreting ages of zircon that are younger than ~1 Ga and the $^{207}Pb/^{206}Pb$ age when interpreting the age of zircon that are older than ~1 Ga. After ~1 Ga, the $^{206}Pb/^{238}U$ age becomes less precise than the $^{207}Pb/^{206}Pb$ age, thus the division in the chronometers (Gehrels 2014).

Multiple studies have found that some non-CA LA-ICP-MS dates are younger and do not overlap within 2σ uncertainty of corresponding CA-ID-TIMS dates (Herriott et al., 2019; Rasmussen et al., 2020; Sharman and Malkowski, 2023). Furthermore, there have been comparisons between CA LA-ICP-MS and non-CA LA-ICP-MS dates from the same samples in which CA LA-ICP-MS dates skew older than non-CA LA-ICP-MS (Crowley et al., 2014; Von Quadt et al., 2014). Watts et al. (2016) also found a similar result between CA and non-CA zircon analyzed via SIMS. However, this trend has not yet been systematically tested across a range of sample characteristics, such as age, location, and type (e.g., sedimentary vs. igneous).

This study aims to assess the degree to which non-CA treated LA-ICP-MS and CA-ID-TIMS dates agree on the same zircon grain across a wide range of samples by creating a database of paired, or tandem, LA-ICP-MS and CA-ID-TIMS U-Pb dates. This study also seeks to understand the causes of discrepancies between LA-ICP-MS and CA-ID-TIMS dates. This research highlights the risk of calculating MDAs from non-CA LA-ICP-MS data, as U-Pb dates that are too young are likely to give incorrect results in age calculations.

Methods

Data sources (academic publications, government studies, etc.) that reported LA-ICP-MS and CA-ID-TIMS U-Pb data from the same zircon grains were collected for input into a database. Depending on the study, CA-ID-TIMS analyses are sometimes preceded by LA-ICP-MS to identify candidate zircon crystals for further analysis. Data sources were identified using several methods that included searching Google Scholar for "CA-ID-TIMS" and other phrases, asking collaborators and CA-ID-TIMS laboratory managers, reviewing published works of laboratory managers, visiting the websites of major CA-ID-TIMS laboratories, and examining studies with published TIMS data in the Puetz et al. (2018) database. Unique identifiers were given to each source, sample, grain, and analysis, and isotopic compositions and corresponding U-Pb and Pb-Pb dates and associated uncertainties were compiled in a relational SQL database. Combining unique sample and grain identifiers allowed analyses from the same grain to be linked (Supplemental Table S1). Some grains are analyzed multiple times and, therefore, are paired more than once. For example, if a grain is dated twice with LA-ICP-MS and once with CA-ID-TIMS, then there are two resulting date pairs. The compilation did not include data sources that lacked a grain identifier that linked CA-ID-TIMS and LA-ICP-MS tables.

U-Pb dates produced via LA-ICP-MS vs CA-ID-TIMS from the same zircon grain are compared by calculating percentage age offset, δ,

$$\delta = \left(\frac{\mu_L - \mu_T}{\mu_T}\right) \times 100$$

where μ_L is the LA-ICP-MS U-Pb date and μ_T is the CA-ID-TIMS U-Pb date. Age offset may also be normalized by measurement uncertainty,

$$\sigma = \left(\frac{\mu_L - \mu_T}{\sigma_L}\right)$$

where σ_L is the absolute 1σ uncertainty of the LA-ICP-MS date. For example, if an LA-ICP-MS date is 100 Ma and its 1σ uncertainty is ±2 Ma, and a CA-ID-TIMS date is 102 Ma, then a σ value of -1 would represent the LA-ICP-MS date being 1 standard deviation removed from the corresponding CA-ID-TIMS date. For samples older than 1 Ga, comparisons are based on the $^{207}Pb/^{206}Pb$ age, or δ_{76}. Correspondingly, the $^{206}Pb/^{238}U$ age was used in computing age offset for samples younger than 1 Ga, or δ_{68}.

Results

In total, there are 1528 date pairs from 1027 unique grains, 49 published studies, from 16 laboratories that provide data (Supplementary Table S1). The dominant laboratories for CA-ID-TIMS analyses are the Boise State University Isotope Geology Laboratory, the ETH Zurich Autonomous Systems Laboratory, and the Berkeley Geochronology Center making up 47%, 24%, and 16% of all CA-ID-TIMS analyses, respectively. The LA-ICP-MS laboratory makeup of the database is as follows, Boise State University Isotope Geology Laboratory accounts for 43% of the total, ETH Zurich Autonomous Systems Laboratory comprises 22%, and the University of Arizona LaserChron Center accounts for 18%. The remaining 13% of CA-ID-TIMS analyses and 17% of LA-ICP-MS analyses are divided between 13 other laboratories (Figs. 2.2B and 2.2C). A total of 49% of the date pairs are from igneous samples, 40% are from sedimentary samples, and the remaining 11% are metamorphic (Fig. 2.2D). Mesozoic zircon are most abundant (44%), followed by Cenozoic (26%), Precambrian (21%), and Paleozoic (9%) (Fig. 2.2A). $^{206}Pb/^{238}U$ date pairs (i.e., samples < 1 Ga) account for 86% of the database.

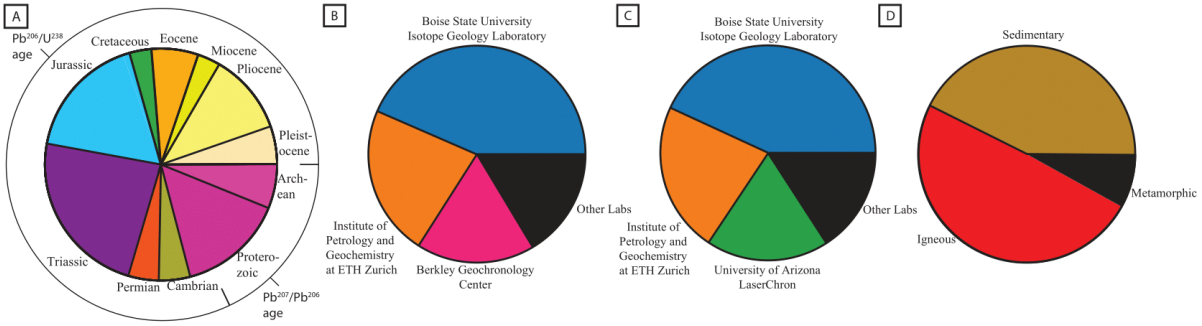

Figure 2.2: Makeup of the database by A) age of samples (age domains are taken from the GSA timescale version 6.0; Walker et al., 2013), B) proportion of CA-ID-TIMS analyses by laboratory, C) proportion of LA-ICP-MS analyses by laboratory, and D) lithologic makeup. The database can be found in Supplemental Table S1.

Figure 2.3 shows all date pairs on a logarithmic scale with a 1:1 trendline. In total, 91% of all date pairs are within ±20% of each other. There are two main groups of outlying points in our dataset that are centered around CA-ID-TIMS dates that are <20 Ma and dates that are >200 Ma. Approximately 28% of these outliers are younger than 20 Ma, and of these date pairs, all that are outside of the ±20% threshold have LA-ICP-MS dates that are older than the corresponding CA-ID-TIMS dates. For example, zircon from a single study that dated the ~1.5 Ma Mesa Falls Tuff exhibited LA-ICP-MS dates that are up to 48 Myr older than the corresponding CA-ID-TIMS dates (Rivera et al., 2016). Similarly, another study that analyzed Tortonian (~10 Ma) tuffs in the Snake River Plain exhibited LA-ICP-MS dates that are 1-20 Myr older than the corresponding CA-ID-TIMS dates (Ellis et al., 2019). Zircon that are this young have very little radiogenic Pb and are thus difficult to measure accurately using LA-ICP-MS (Zi et al., 2022). All zircon between 20 and 200 Ma fall within the ± 20% envelope, and 6.6% of zircon older than 200 Ma fall outside of ±20%.

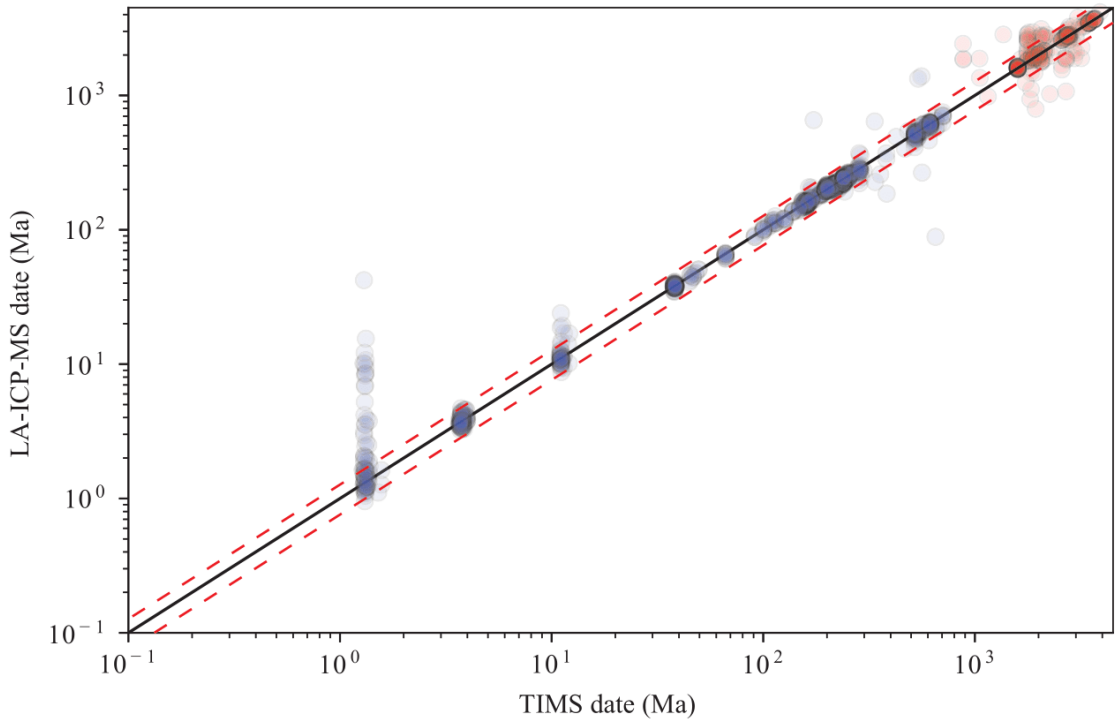

Figure 2.3: Scatterplot of data on a logarithmic scale with a 1:1 trendline. Dashed lines represent +/- 20% age offset between LA-ICP-MS and CA-ID-TIMS analyses. Data points that are blue and red represent $^{206}Pb/^{238}U$ and $^{207}Pb/^{206}Pb$ dates, respectively

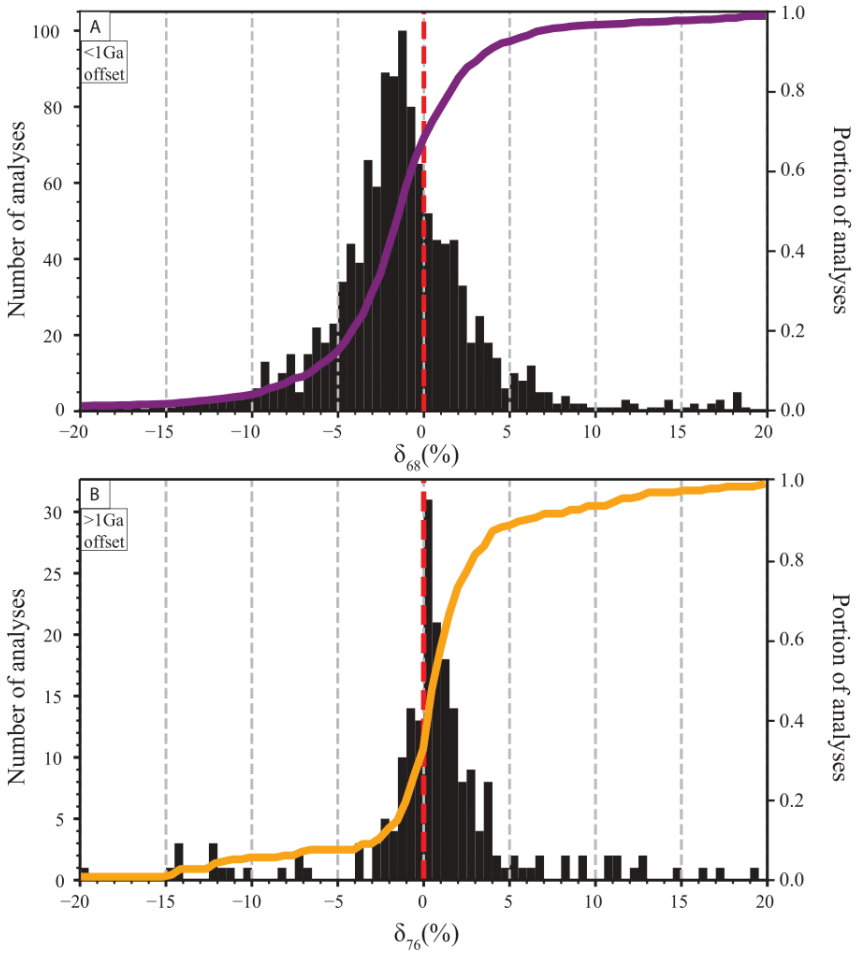

Figure 2.4: Histograms and cumulative distribution functions showing the age offset of all LA-ICP-MS and CA-ID-TIMS date pairs within ±20%. A.) Values of δ_{68} for analyses younger than 1 Ga. B.) Values of δ_{76} for analyses older than 1 Ga.

For zircon younger than 1 Ga, 74% of δ_{68} values are <0% (i.e., the LA-ICP-MS date is younger than the corresponding CA-ID-TIMS date). The mode of the δ_{68} distribution is between -2% and -2.5% (Fig. 2.4). For zircon that are >1 Ga, approximately 65% of δ_{76} values are >0%, with a mode between 0 and 0.5% (Fig. 2.4). For zircon that are > 1 Ga, the mode of δ_{68} falls between -0.5% and -1% offset.

When $^{206}Pb/^{238}U$ dates (samples < 1 Ga) are subdivided by lithology, 77% of δ_{68} values for sedimentary zircon are <0%, with the mode of the δ_{68} distribution falling between -2.5% and -3% (Fig. 2.5). About 65% of δ_{68} values for igneous zircon have negative values, with a mode between -1.5% and -2%. The mode of the distribution of δ_{68} for metamorphic zircon is positively shifted between 0% and 0.5%, and 54% of δ_{68} values are >0%. However, there are far fewer date pairs (n=123) for metamorphic zircon than for sedimentary or igneous zircon (n=611 and n=794, respectively) (Fig. 2.2). Figure 2.6A shows that the offset of σ_{68} is negatively shifted, with a mode between -0.75 and -1.0 standard deviations. The distribution of σ_{76} values has a mode of about 0.5σ, and ~77% of date pairs have a positive offset (Fig. 2.6b). For $\sigma_{68,}$ 38.4% of date pairs are greater than ±2σ of each other, for σ_{76} that number increases to 60%.

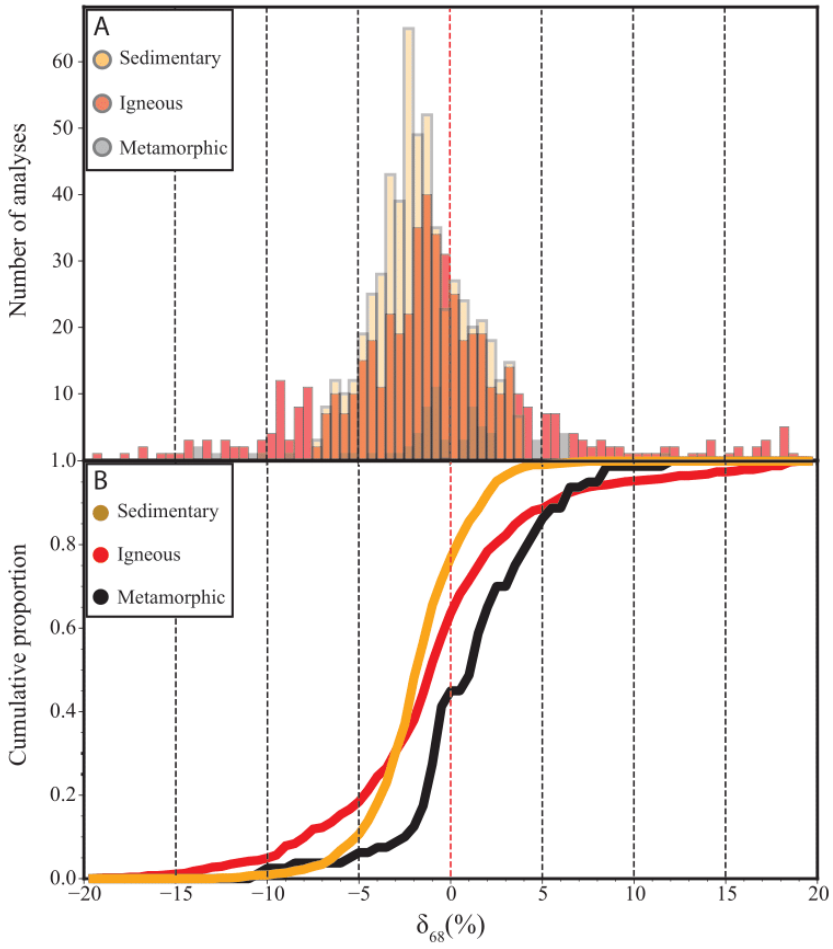

Figure 2.5: δ_{68} of all LA-ICP-MS and CA-ID-TIMS date pairs <1 Ga by lithology type. δ_{68} values >20% and <-20% are not shown.

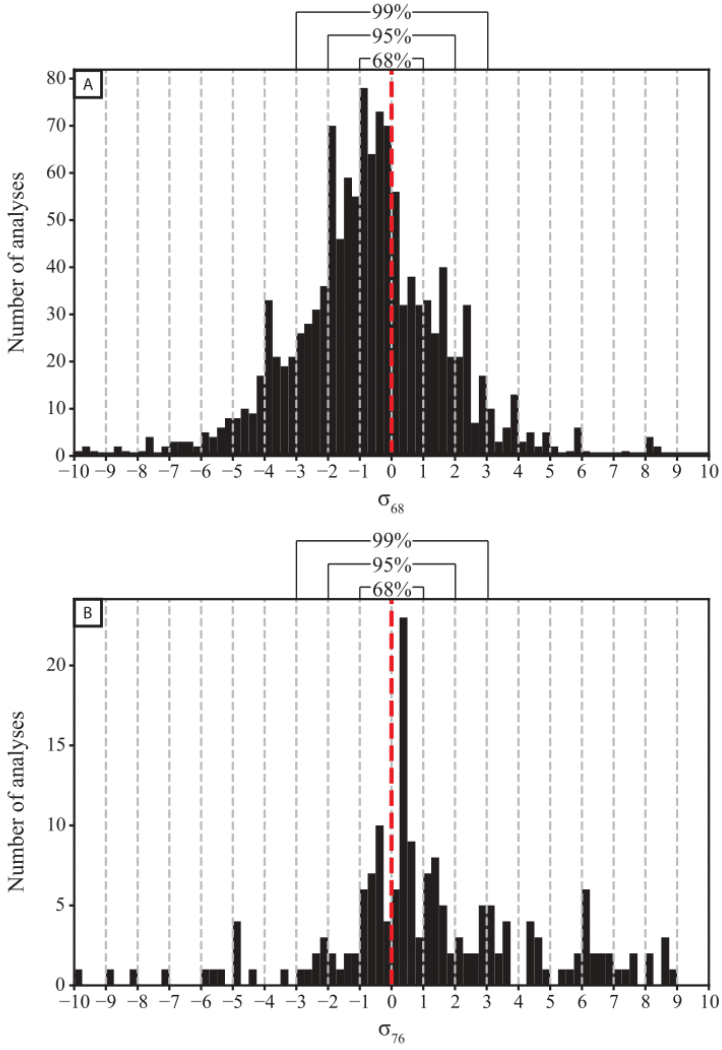

Figure 2.6: Histogram showing the number of standard deviations between LA-ICP-MS and CA-ID-TIMS dates. A) $^{206}Pb/^{238}U$ date pairs younger than 1 Ga. B) $^{207}Pb/^{206}Pb$ date pairs older than 1 Ga. At the top are brackets that show the percentage of data that would be present for a normal distribution.

Discussion

Causes of discrepancy between LA-ICP-MS and CA-ID-TIMS

Why are $^{206}Pb/^{238}U$ dates acquired via LA-ICP-MS systematically younger than their corresponding CA-ID-TIMS dates on the same zircon? One possible explanation is that variations in δ_{68} reflect imprecision associated LA-ICP-MS measurements (Schoene et al., 2013a). However, several considerations suggest that this explanation is unlikely to be the sole contributor to differences between LA-ICP-MS and CA-ID-TIMS dates. Both σ_{68} and σ_{76} show that LA-ICP-MS U-Pb and Pb-Pb dates are over-dispersed relative to CA-ID-TIMS. For instance, if U-Pb and Pb-Pb date dispersion were due to measurement uncertainty alone, then we would expect σ_{68} and σ_{76} to follow a normal distribution where 68% of all date pairs should be within 1σ, 95% within 2σ, and 99% within 3σ (Fig. 2.6). Instead, only 61.6% of $^{206}Pb/^{238}U$ date pairs are within ±2σ of each other (samples < 1 Ga) and only 40% of $^{207}Pb/^{206}Pb$ date pairs are within ±2σ of each other (samples > 1 Ga). Furthermore, if variations in δ_{68} values were due to analytical uncertainty alone, then we would expect negative and positive values to be approximately evenly split, which is not the case. Thus, analytical uncertainty is unlikely to be the sole cause for discrepancies between LA-ICP-MS and CA-ID-TIMS dates.

What additional factors, beyond analytical uncertainty, might result in a systematic negative offset in δ_{68} values? I consider three possible causes: systematic biases with between unknowns and standards in LA-ICP-MS analyses ("matrix effects"; Sliwinski et al., 2017), inheritance (Gehrels, 2014), and Pb loss (Black, 1987).

Matrix effects are a known analytical bias that refers to the impact of differences in zircon matrix properties between standards and unknowns on the accuracy and precision of radiometric dating (Black et al., 2004; Allen and Campbell, 2012). Zircon crystals contain trace amounts of

radioactive elements and those trace elements emit alpha particles during radioactive decay (Murakami et al., 1991; Solari et al., 2015). These alpha particles in total can damage the crystal structure to different degrees, causing variations in laser-induced element fractionation (LIEF) between standards and unknowns (Sliwinski et al., 2017). LIEF comes from the differing rate of change in the $^{206}Pb/^{238}U$ ratio during ablation (i.e., downhole fractionation). So, when LA-ICP-MS analyses are corrected based on standards, differences in LIEF can cause a systematic bias in $^{206}Pb/^{238}U$ ages (Marillo-Sialer et al., 2016). Sliwinski et al., (2017) found that matrix effects are most pronounced in younger zircon (Cenozoic) because of the lower alpha dose when compared to standards used and produce LA-ICP-MS dates that are too young or, in the context of this study, negatively shifted.

There are multiple ways to correct for matrix effects in zircon including an alpha dose correction based on the amount of U and Th and the age of a zircon (Sliwinski et al., 2017). Thermal annealing zircon in air at ~900^{o}C has also been shown to reduce the influence of matrix effects (Allen and Campbell, 2012; Hao et al., 2021). Although thermal annealing is not consistently practiced between LA-ICP-MS laboratories, the majority of the LA-ICP-MS data in this study were thermally annealed prior to analysis. Because the magnitude of the negative offset in δ_{68} values is greater than expected for matrix effects on thermally annealed zircon (Slinwinski et al., 2017), it seems unlikely that matrix effects are the predominant cause for the shift in our data. In addition, the offset is not exclusive to Cenozoic grains but is also present in Mesozoic and older zircon, whereas matrix effects mainly cause a negative offset in Cenozoic grains (Slinwinski et al., 2017).

Zircon crystals grow outward from their origin and can have multiple age domains due to different crystal growth periods (Gehrels, 2014). The incorporation of these older age domains in

an analysis is called inheritance. Inheritance would be more likely to make the CA-ID-TIMS date older than the corresponding LA-ICP-MS date. This is because LA-ICP-MS analyses use discrete ablations of a portion of a zircon crystal whereas the entire grain or a fragment of the grain must be dissolved into a solution prior to analysis via CA-ID-TIMS, thus representing an average date of the dissolved material (Gehrels, 2014). Zircon analyses that experience inheritance often have high discordance values (Gehrels, 2014) that may cause them to be discarded by the lab or by the author of the given study. However, inherited cores from a melt that has gone through multiple stages of evolution might be only modestly older than the younger portion of the crystal, and thus not highly discordant (Schoene et al., 2013). Zircon mounts are routinely observed with cathodoluminescent (CL) imaging, allowing users to select zircon without obvious inherited cores (Hanchar and Miller, 1993; Yuguchi et al., 2023). Because commonly practiced screening techniques and discordance filters that would likely identify most zircon with inherited cores, I consider it unlikely that inheritance is the predominant cause for the negative shift in δ_{68} However, inheritance is possibly a contributing factor in the offset of δ_{68}.

Pb loss causes a decrease in the $^{206}Pb/^{238}U$ ratio which makes a zircon appear too young (Gehrels, 2014). The comparison in this study is between non-CA LA-ICP-MS and CA-ID-TIMS. Chemical abrasion is known to remove zones that have experienced Pb loss, so it is reasonable to expect that non-CA LA-ICP-MS dates are susceptible to measuring these zones that do have Pb loss (Mattinson, 2005, 2010; Schoene et al., 2013a; Corfu, 2013). Other studies have noted that chemically abrading zircon before LA-ICP-MS and SIMS results in dates that are older than that of non-CA analyses (Von Quadt et al., 2014; Watts et al., 2016). If the Pb loss occurred recently, then the $^{207}Pb/^{206}Pb$ ratio will not be modified as neither ^{207}Pb nor ^{206}Pb are preferentially removed (Dicken, 1995). The negative shift is only manifested in δ_{68} (samples <1 Ga) and not in δ_{76}

(samples >1 Ga). If inheritance were to blame, it is expected that both ratios to be affected. Instead, the preferential influence on the U-Pb dates is suggestive that Pb loss is likely a more important factor. Unlike inheritance, which often involves mixing of a rim with a much older core, Pb loss can be much more discrete, and the inaccurate U-Pb age could go unnoticed.

It is readily observable that there are differences in δ_{68} between detrital and igneous zircon (Fig. 2.5). A possible cause for the LA-ICP-MS dates <1 Ga being more offset from their CA-ID-TIMS dates in detrital rather than igneous zircon is the intentional bias inherent in picking the youngest zircon after LA-ICP-MS analyses. Detrital studies that target young zircon for MDA analysis usually use LA-ICP-MS as a prescreening technique, and then subsequently date the youngest zircon with CA-ID-TIMS (Schaltegger et al., 2015; Cox et al., 2018; Herriott et al., 2019; Schwartz et al., 2023). Dates that appear young in non-CA LA-ICP-MS analyses are more likely to have undergone Pb loss. After being analyzed with CA-ID-TIMS analyses, the zircon will have likely been treated with chemical abrasion and be dated older than their LA-ICP-MS date. In studies focusing on igneous rocks, authors do not usually prioritize the youngest zircon for analysis, but instead are more likely to analyze zircon with a range of LA-ICP-MS dates (Gaschnig et al., 2010; Keeley et al., 2013).

Implications for maximum depositional age calculations using LA-ICP-MS

These results have implications for maximum depositional age (MDA) calculations, particularly as an MDA calculated from LA-ICP-MS dates is likely to be younger than an MDA calculated from CA-ID-TIMS dates. Though a negative age offset of ~2% may not seem like much, this magnitude of inaccuracy could lead to erroneous interpretations. Take the example of constraining the Cambrian-Ordovician boundary (485.4 Ma) with the youngest single grain (Walker et al., 2013). Given a true age of 485.4 Ma, a LA-ICP-MS date that is 2% younger would

yield a date of 475.7 Ma, which is two stages on the geologic time scale younger than the correct date. For a slightly more conservative MDA calculation, like the youngest cluster of analyses that overlap at 1σ or 2σ, there only needs to be two to three zircon, respectively, that exhibit negative age offsets to make a similarly too-young MDA (Herriott et al., 2019; Rasmussen et al., 2020, 2021). Because it is common for LA-ICP-MS dates to exhibit considerably less than -2% age offsets, it is anticipated that MDAs that use LA-ICP-MS dates alone are unlikely to be as precise or accurate are CA-ID-TIMS analyses of those same zircon grains. This study highlights the risk of selecting the youngest single grain as an MDA using LA-ICP-MS data alone (Copeland, 2020). It is possible that calculating MDA on U-Pb dates acquired via CA-LA-ICP-MS will have a beneficial effect on MDA accuracy as CA prior to LA-ICP-MS improves both resolution and percentage of concordance with younger and older zircons, respectively (Donaghy et al., 2023).

Conclusions

In this study, I have assessed the degree of agreement between LA-ICP-MS and CA-ID-TIMS U-Pb dates from the same zircon crystals. The data I compiled has come from multiple laboratories, although the majority (65%) of data came from Boise State University or ETH Zurich. I have found that there is a systematic negative shift in $^{206}Pb/^{238}U$ dates acquired via LA-ICP-MS relative to CA-ID-TIMS. $^{207}Pb/^{206}Pb$ dates (zircon >1 Ga) are not observed to have a shift between LA-ICP-MS dates and its corresponding CA-ID-TIMS date.

Pb loss is likely the primary mechanism for the offset in δ_{68} rather than "matrix effects" or inheritance. Matrix effects can be mitigated, at least in part, with thermal annealing, or with an alpha dose correction. Inheritance is unlikely to be the primary cause for the offset in δ_{68} due to the lack of a complimentary offset in δ_{76} and the regular avoidance of zircon with multiple age domains through CL imaging. While it is suggested that Pb loss is the leading factor for δ_{68} offset,

it is possible that other analytical or geological factors (e.g., matrix effects, inheritance) may also contribute to a systematic negative shift in δ_{68}.

Age offset varies by the lithology of the host rock. Sedimentary zircon are more likely to yield a LA-ICP-MS date that is younger than it's corresponding CA-ID-TIMS date (73% of date pairs) versus igneous zircon (60% of date pairs). The mode the δ_{68} distribution in igneous zircon is ~-1.5 to -2%, whereas the mode for detrital zircon is ~-2.5 to -3%. It is likely that the cause for the increased offset in detrital studies is from the selection of younger zircon in MDA studies, as these youngest zircon are more likely to have undergone Pb loss. This work has implications for understanding the accuracy of non-CA LA-ICP-MS relative to CA-ID-TIMS. This study highlights a need for further study of applications of CA techniques to LA-ICP-MS or other approaches that mitigate the effects of Pb loss on non-CA LA-ICP-MS data.

Chapter 3: Maximum depositional age analysis of the Elliot Formation: Tandem LA-ICP-MS and CA-ID-TIMS dating of zircon at Barkley Pass, South Africa

Introduction

The Late Triassic to Early Jurassic was a pivotal time for Earth's geologic and biotic history. Early diversification, evolution, and proliferation of Dinosauria, the eruption of the Central Atlantic Magmatic Province (CAMP; 201.566-200.916 Ma), the end-Triassic extinction (ETE) (201.564 ± 0.015 Ma), and the Triassic-Jurassic Boundary (TJB) (201.464 ± 0.004 Ma) all occurred within a few hundred thousand years of each other (Bordy et al. 2004c; Blackburn et al., 2013). The Triassic-Jurassic Elliot Formation is a fluvial succession deposited in high latitudes of the southern hemisphere (paleolatitude of ~40 degrees south; Olsen and Galton, 1984) and contains a plethora of early dinosauria as well as a variety of pseudosuchian vertebrate fossils deposited throughout the basin (McPhee and Choiniere 2016; Bordy et al. 2017; McPhee et al. 2017; Wills et al. 2018; Barrett et al. 2019; Chapelle et al. 2019; Tolchard et al. 2019). The Elliot Formation is also likely one of the most complete high-latitude terrestrial sedimentary units that may reflect influences of the CAMP volcanism in the southern hemisphere (Bordy et al., 2004b; Blackburn et al., 2013).

The Elliot Formation is informally divided into two subunits: the lower Elliot Formation (LEF) and the upper Elliot Formation (UEF) (Bordy et al., 2004b). The LEF and UEF are currently characterized by the *Scalenodontoides* assemblage range zone and the *Massospondylus* assemblage range, respectively, that constrain the age of the Elliot Formation to range from Norian to Sinemurian (Tolchard et al., 2019; Viglietti et al., 2020). The North American, low-latitude Moenave Formation also records the TJB, the ETE, and influence of CAMP volcanism in a similar fluvial succession (Boudreaux, 2019; Mmasa, 2021; Oefinger, 2021); this research provides the

geochronological framework for comparing the Elliot Formation with the time equivalent Moenave Formation. To best understand the worldwide effects of CAMP volcanism on climate and the paleo-biosphere, geochronological age constraints on the Elliot Formation are needed.

The Triassic-Jurassic Elliot Formation has been well characterized through the study of magnetostratigraphy and lithostratigraphy (Bordy and Eriksson 2015; Sciscio et al., 2017). Despite previous studies, there is a lack of absolute age constraints and chemostratigraphy data collected from the Elliot Formation. Few studies have conducted detrital zircon geochronology on the Elliot Formation, with the first detrital zircon dates published by Bowden (2013) and the first study of its maximum depositional age (MDA) recently conducted by Bordy et al. (2020). Bordy et al. (2020) produced high-resolution CA-ID-TIMS dates from four samples in their study. To build on the work of Bordy et al. (2020), I have sampled vertically through Barkley Pass (Fig. 3.1) rather than discretely sampling throughout the basin with the goal of establishing a robust age model for the Elliot Formation in the southern part of its outcropping range. The outcropping section at Barkley Pass is the thickest known and is the type section of the Elliot Formation. Sampling the type section at Barkley Pass allows for high resolution sampling for both chemostratigraphy and detrital zircon that can be used in correlations with non-type sections throughout the basin. Barkley Pass is less fossiliferous than other sections of the Elliot Formation and is by consequence less biostratigraphically constrained (McPhee et al., 2017; Sciscio et al., 2017; Viglietti et al., 2021). Recently collected chemostratigraphy samples show the onset of a significant $\delta^{13}C_{org}$ excursion at 154 m above the base of the measured Elliot Formation exposure, interpreted to be the onset of the ETE (Oberg, 2023).

The new CA-ID-TIMS U-Pb dates from zircon demonstrate an upwards-younging trend at Barkley Pass, with the oldest sample yielding a date of 208.80 ± 0.14 Ma (~16 m above the start

of exposures) and the youngest sample yielding a date of 194.65 ± 0.13 Ma (~5 m below the contact with the Clarens Formation). The proportion of near depositional age zircon (<220 Ma) increases from 7% to 36%, on average, in samples handpicked for sharp, euhedral crystal facies versus being randomly selected. My data support the preliminary placement of the ETE based on precursory carbon-isotope results obtained by PhD candidate Danielle Oberg at 154 m above the base of the Elliot Formation at Barkley Pass. Additionally, my data indicate that the location of the TJB is within the uppermost LEF, and not at the boundary between the LEF and UEF as previously suggested by other researchers (Bordy et al., 2020).

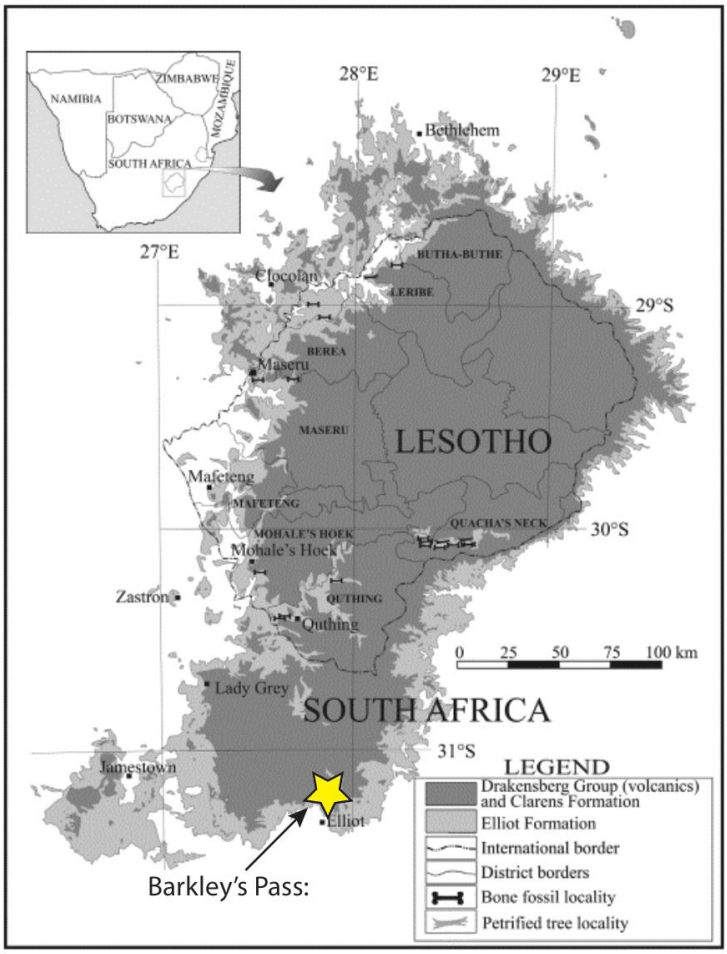

Figure 3.1: Approximate location of the type section, Barkley Pass, and the outcrop distribution of the Elliot Formation and overlying units in and around South Africa and Lesotho (modified from Bordy et al., 2004b).

Geological Background

The Elliot Formation is the second youngest unit of the Stormberg Group in the Main Karoo Basin (MKB) in South Africa and Lesotho (Bordy et al., 2020). The Elliot Formation is bounded by the upper Triassic Molteno Formation at its lower boundary and is conformable with the overlying Clarens Formation. The biostratigraphy, lithology, and magnetostratigraphy of the Elliot Formation have been well-established (Bordy, 2004a; Bordy et al., 2004b; Sciscio et al., 2017). In contrast, the provenance and detrital zircon U-Pb geochronology of the Elliot Formation have only been loosely constrained (Veevers et al., 1994; Bordy et al., 2020). The Stormberg Group is interpreted to have two major source areas: the Cape Fold Belt (CFB) and the Kalahari Craton (Veevers et al., 1994; Bordy et al., 2004a). Bordy et al. (2004a) conducted the first detailed provenance work on the Elliot Formation and found that recycled sediments from the CFB are likely dominant in the Elliot Formation. The Elliot Formation lacks primary volcaniclastic tuffs, but rare tuffaceous siltstones and highly chemically altered bentonites are interpreted to have been sourced from southwestern Gondwana in present-day South America (Bordy and Abrahams, 2016; Bordy et al., 2020).

The LEF is interpreted to be a fining-upwards fluvial succession that was directly sourced from the CFB. The LEF is dominated by very fine-grained, maroon sandstones and mudstones with interbedded tan, fine to medium-grained channel sandstones. The UEF lithologic composition is silty, very fine-grained, brick-red sandstones and mudstones with occasional interbedded, well-sorted, fine sandstones (Figs. 3.2). The UEF is interpreted to include an increased amount of source material coming from the Kalahari Craton with gradually increasing eolian sourced sediments up section, in line with the desertification of Gondwana (Veevers et al., 1994; Bordy et al., 2004b). In the Late Triassic, southern Gondwana was undergoing major desertification north of the study area

(Bordy et al., 2004c). Desertification gradually spread south during the Early Jurassic, changing the facies from the UEF to the overlying Clarens Formation (Veevers et al., 1994). The Clarens Formation is the uppermost unit in the Stormberg group, composed of thickly bedded aeolian sandstones with dune scale cross beds, and is overlain by flood basalts of the Drakensburg group (Bordy and Head, 2018).

Figure 3.2: Stratigraphic column of the Elliot Formation at Barkley Pass. Detrital zircon samples are noted. Only CA-ID-TIMS dates are shown.

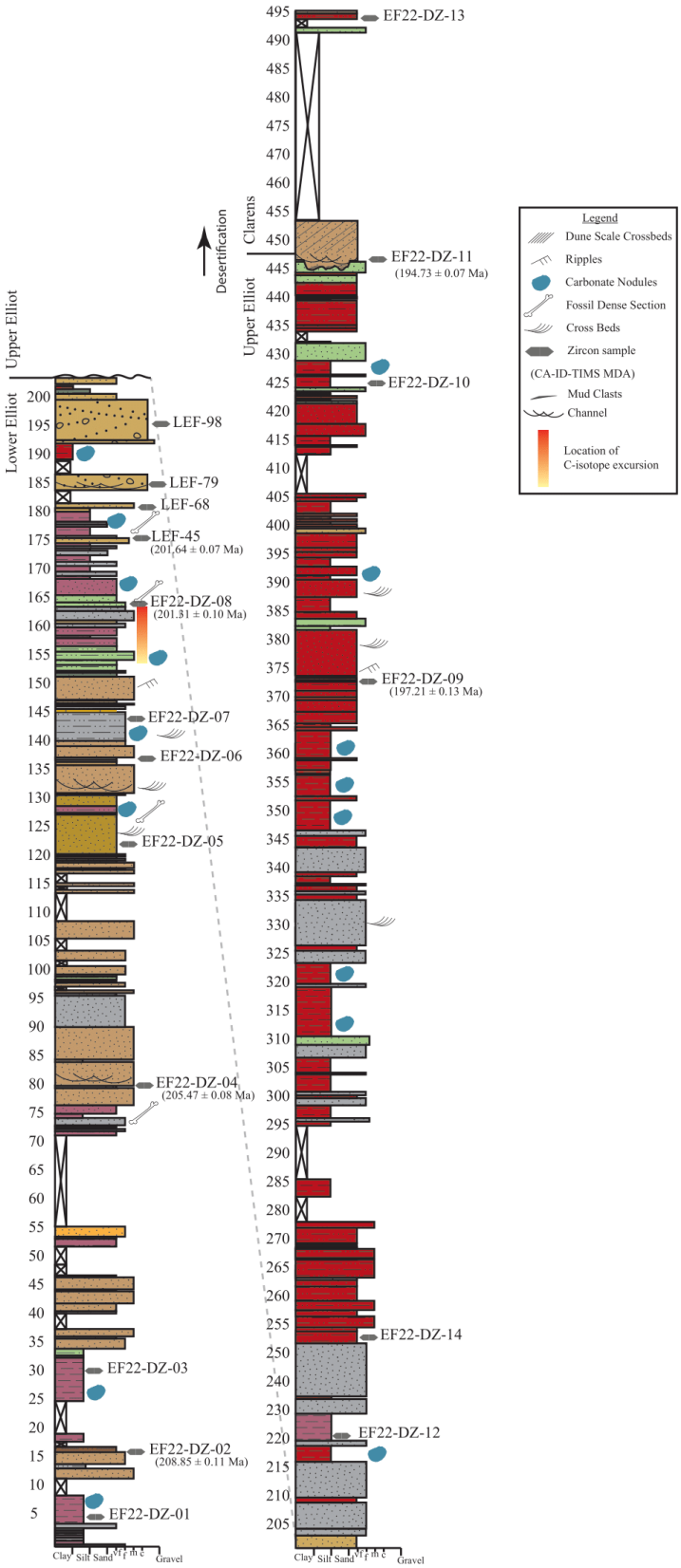

A synthesis of chronostratigraphic constraints for the Elliot Formation was published by Bordy et al. (2020) who constrained the MDA of 15 tuffaceous siltstones and sandstones in the Elliot Formation, primarily with LA-ICP-MS data. Ten samples were taken in the LEF, three of which had CA-ID-TIMS analysis. The UEF had five samples with one sample being dated with CA-ID-TIMS. Bordy et al. (2020) also constrained their basal sample in the LEF to 211.5 ± 2.8 Ma with LA-ICP-MS data and the top of the LEF to 204.9 ± 0.88 Ma from CA-ID-TIMS; likewise, the top of the UEF is constrained with an MDA of 191.1 ± 1.5 Ma from CA-ID-TIMS data. Veevers et al. (1994) only reported randomly selected zircon dates that did not yield U-Pb dates younger than 220 Ma. I processed four samples that were collected from Barkley Pass in 2019 and 14 samples in 2022. Two samples (EF22-DZ-01 and -10) yielded insufficient amounts of zircon to be analyzed via LA-ICP-MS. Because of low zircon yield, samples EF22-DZ-05, -06, and -13 do not have random analyses and sample EF22-DZ-03 does not have handpicked analyses. All other samples have been analyzed from random and handpicked fractions with LA-ICP-MS. A total of six samples were selected for further analysis via CA-ID-TIMS.

Methods

Sampling locations from the Elliot Formation were chosen based on stratigraphic position and lithology. Samples were chosen to span the base to the top of the Elliot Formation but with higher resolution sampling near the suspected location of the TJ boundary near the LEF and UEF contact (Bordy et al., 2020). Spacing between samples ranged from 9 m to 117 m with an average of 29 m (Table 3.1). Various lithologies were collected to increase the diversity of grain sizes and depositional environments sampled. Targeted lithologies included very fine-grained fluvial channel sandstones, maroon silty to very fine-grained sandstones, massive maroon mudstones, and olive-gray silty very fine-grained sandstones (Supplementary Table S2).

Samples collected from Barkley Pass consisted of 2.25-4.5 kg of raw samples that were processed to extract detrital zircon grains using the following processes: jaw crushing the bulk rock; disc milling the crushed pieces to sand-sized particles; washing sand particles with water to remove clays, unstable, and low-density minerals with a blue bowl separator; separating magnetic grains with a hand magnet and then a slope Frantz magnetic barrier laboratory separator; and separating dense grains (>3.3 g/cm^3) with methylene iodine (MEI). Zircon grains were then split into a random, unbiased fraction and a fraction that was handpicked for sharp, euhedral zircon.

The random zircon separate was mounted on double-sided sticky tape and analyzed via LA-ICP-MS at the University of Arkansas Trace Element and Radiogenic Isotope Laboratory (TRAIL). The TRAIL uses a Thermo-iCap-Q connected to the ESI 193nm Excimer Laser Ablation System with a 25-micron spot size at 10 Hz and a helium flow rate of 0.8 L/min (Giles et al. 2023). Raw data was then reduced using the Iolite 4 data reduction software. Data was filtered for discordance and uncertainty as follows: analyses that are <1 Ga with a $^{206}Pb/^{238}U$ vs $^{207}Pb/^{235}U$ discordance >15% or >10% uncertainty at 2σ, analyses >1 Ga were filtered if >30% or <-15% discordant ($^{206}Pb/^{238}U$ vs $^{207}Pb/^{206}Pb$). Age interpretations are based on $^{207}Pb/^{206}Pb$ if the $^{206}Pb/^{238}U$ date is older than 1 Ga.

Zircon from the handpicked split were selected under a microscope for sharply faceted grains to improve the yield of zircon of near-depositional age (<220 Ma), which will better constrain the sample's maximum depositional age (Fekete et al., 2023). After handpicking, the samples were mounted in epoxy and polished to expose the zircon's core at the Boise State University Isotope Geology Laboratory (BSU-IGL) to be first analyzed by LA-ICP-MS and then CA-ID-TIMS. For LA-ICP-MS, the BSU-IGL uses an iCAP RQ Quadrupole ICP-MS and Teledyne Photon Machines Analyte Excite+ 193 nm excimer laser ablation system with a laser

spot size of 15-micron at 10 Hz and a 0.25 L/min helium gas flow rate. For CA-ID-TIMS, the BSU-IGL dissolves zircon with two iterations of 120 ml of 29 M HF for 12 hours at 190°C and, 120 ml of 6M HF. Isotopic measurements were made on a GV Isoprobe-T multicollector thermal ionization mass spectrometer, equipped with an ion-counting Daly detector. The BSU-IGL filters LA-ICP-MS data for 5% discordance. The age interpretation was based on $^{207}Pb/^{206}Pb$ for dates older than 1 Ga.

The LA-ICP-MS data from the handpicked zircon separates was used to prioritize samples for further CA-ID-TIMS analysis. CA-ID-TIMS analyses were selected from handpicked aliquots after being analyzed by LA-ICP-MS. Grains were selected based on low discordance values and young dates. Between 4-6 of the youngest grains were removed from the epoxy mount and broken into two fragments provided the zircon was large enough.

Using detritalPy, eight MDA approximations are calculated for my LA-ICP-MS dates: youngest single grain (YSG), youngest cluster with overlapping uncertainties at 1σ (YC1σ), youngest cluster with overlapping uncertainties at 2σ (YC2σ), youngest three zircons (Y3Zo), a weighted average of the youngest three zircon dates that overlap within uncertainty (Y3Za), the youngest graphical peak (YPP) of the probability density plot (PDP), the youngest statistical population (YSP), and the tau (τ) method (Sharman et al., 2018; Sharman and Malkowski, 2020). One additional MDA calculation method was added from Vermeesch (2021), which is the Maximum Likelihood Age (MLA).

MDA calculations from CA-ID-TIMS data were based on either the weighted mean of multiple grains (if they overlapped at 2σ uncertainty) or the youngest single grain if an overlapping cluster was absent. In two cases, the archived fragment of the youngest grain was analyzed to assess intra-grain consistency (Fig. 3.3). The MDA of sample EF22-DZ-09 is interpreted based on

a single analysis of the YSG. The MDAs of the other five samples are based on weighted means of multiple grains (WMA) and/or separate analyses of fragments from the youngest grain (Fig. 3.3).

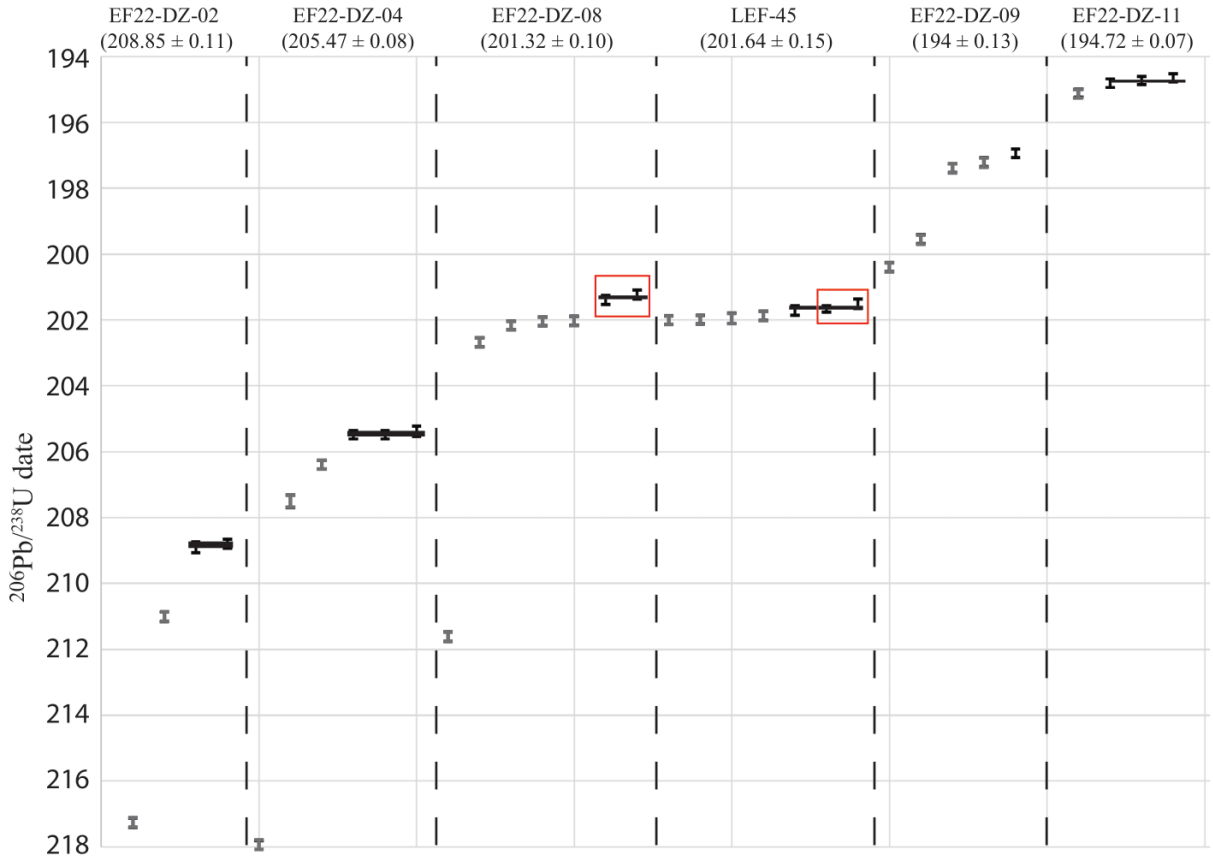

Figure 3.3: Ranked date plot of CA-ID-TIMS analyses and preferred MDAs. Black analyses were used in calculating the MDA. Dates in the red boxes are fragments of the same zircon.

Results

Random LA-ICP-MS U-Pb analyses

Between 43 and 164 U-Pb analyses are reported for randomly analyzed samples, with an average of 135. Nearly 7% of all random dates are near depositional age (<220 Ma). Major age peaks tend to occur between 190-250 Ma, 500-600 Ma, and 1000-1100 Ma (Fig. 3.4). Randomly

analyzed samples in the LEF tend to have less discrete age modes than UEF samples. The largest portion of zircon (up to 40% depending on the sample) is 500-600 Ma. Of randomly analyzed aliquots, 75% have a YSG that is near depositional age (i.e., <220 Ma).

Handpicked LA-ICP-MS U-Pb analyses

Between 8 and 81 U-Pb analyses are reported for handpicked samples, with an average of 36. At the extremes, there are five-times the number of near depositional age zircon in handpicked aliquots versus random (Table 3.1). The average proportion of near depositional age grains is ~36% in handpicked aliquots. Of the UEF handpicked samples, 43% of zircon were near depositional age, which is 17% higher than that of handpicked sample in the LEF (25%). Age modes in handpicked aliquots are relatively similar to that of random aliquots, except for age modes >700 Ma, which are distinctively scarcer in the handpicked results (Fig. 3.5). All the YSGs of the handpicked aliquots are near depositional in age but do not show a clear upwards-younging trend (Table 3.1). Of the 15 handpicked samples from Barkley Pass analyzed with LA-ICP-MS, 14 have an MLA MDA that is near depositional age, 12 have near depositional MDAs from YC1σ, and ten have near depositional MDAs from YC2σ (Table 3.1). Other, less conservative MDA calculations like Y3Za, Y3Zo, and YPP produce, at best, nine samples with MDAs that are near depositional age. The τ method also provides nine samples with near depositional MDA calculations.

CA-ID-TIMS U-Pb analyses

A total of six samples were analyzed via CA-ID-TIMS. All but one of the 34 zircon grains analyzed by CA-ID-TIMS are <220 Ma. The six samples at Barkley Pass (EF22-DZ-02, -04, -08, -09, -11, and LEF-45) that were analyzed by CA-ID-TIMS show an upwards-younging trend in the YSG, except for LEF-45, which was dated to 201.64 ± 0.15 Ma, making it 0.32 Ma older

than the underlying CA-ID-TIMS date (EF22-DZ-08). LEF-45 and EF22-DZ-08 are dated with a weighted mean average from multiple grain fragments from the YSG analyzed. EF22-DZ-02 was dated to 208.85 ± 0.11 Ma from a weighted mean average of two zircon, and 66 m up section, EF22-DZ-04 was dated to 205.47 ± 0.08 Ma with a three-grain weighted mean average. The uppermost sample in the LEF, EF22-DZ-08, is dated to 201.32 ± 0.10 Ma and is 162 m from the base of the section of the LEF. The YSG from EF22-DZ-09, 361.55 m (170 m from the LEF-UEF contact) from the base of the section, and the first UEF CA-ID-TIMS data, is dated to 196.94 ± 0.13 Ma. Finally, EF22-DZ-11, the uppermost sample which is 420.55 m from the base of the Elliot Formation, is dated to 194.73 ± 0.07 Ma with a weighted mean average from three zircon.

MDA calculations

MDA calculations on random samples are drawn from more analyses than the handpicked samples (average of 135 analyses for random samples versus 36 in handpicked samples). Despite this, the proportion, and often number, of dates that are near depositional age remains higher in handpicked samples (Supplementary Table S2). Five of the 12 samples (42%) with random analyses have MDAs from YC1σ, YC2σ, Y3Zo, YPP, and YSP that are near depositional age (Table 3.1). Three samples have a near depositional age MDA from the τ method, and six samples have near depositional MDAs from Y3Za. Seven of 12 samples' MLA calculations are near depositional age. For the MDAs from handpicked aliquots calculated with YC1σ and YPP, 12 out of 15 are near depositional age. Y3Za has 12 samples dated to near depositional age. YC2σ, Y3Zo, and YSP all have 10 samples that are near depositional MDAs, and the τ method has seven samples that are near depositional age. Handpicked aliquots calculated with MLA have 14 samples that are near depositional age.

Figure 3.4: Cumulative distribution functions (CDFs) and kernel density estimations (KDEs) of LA-ICP-MS U-Pb results. KDEs are filled for the handpicked results, and young zircon (<220 Ma) are shaded in red. KDE bandwidth = 10 Ma. np: number of picked analyses, nr: number of random analyses.

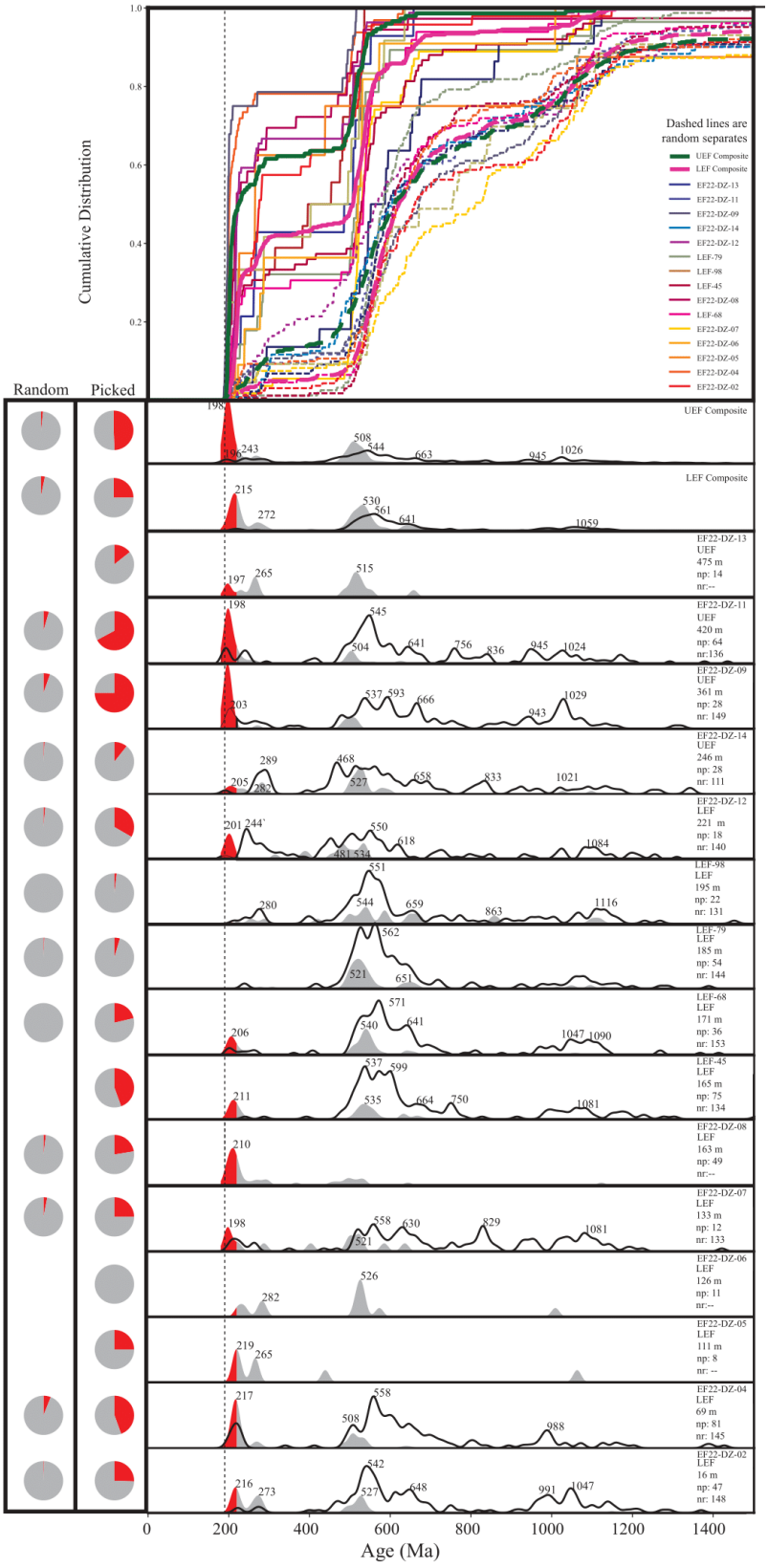

LA-ICP-MS (Picked)																													
Sample	Thickness (m)	N	YSG	±2σ	YC1s	±2σ	MSWD	N	YC2s	±2σ	MSWD	N	Y3Za	±2σ	MSWD	Y3Zo Ma	±2σ	MSWD	YPP	YSP	±2σ	MSWD	N	tau	±2σ	MSWD	N	MLA	±2σ
EF22-DZ-13	475.3	14	195.00	5.02	197.45	3.06	1.56	2	265.57	3.98	0.75	3	203.78	2.75	42.98	265.57	3.98	0.75	198.20	265.57	3.98	0.75	3	265.57	3.98	0.75	3	197.17	3.4
EF22-DZ-11	420.6	64	189.00	7.88	193.48	1.54	0.25	17	196.16	1.13	1.05	32	190.38	4.30	0.09	191.75	3.33	0.42	196.30	196.24	1.12	1.03	34	197.95	1.04	2.59	41	196.63	1.2
EF22-DZ-09	361.6	28	188.00	4.51	189.49	2.89	0.41	3	192.88	1.53	1.19	9	189.49	2.89	0.41	189.49	2.89	0.41	194.60	192.71	1.56	1.02	9	195.87	1.19	3.13	21	195.21	1.3
EF22-DZ-14	246.6	28	192.00	9.22	207.26	6.11	0.40	2	202.47	5.06	3.96	3	202.47	5.06	3.96	202.47	5.06	3.96	207.40	207.26	6.11	0.40	2	284.92	5.65	0.13	3	192.60	14.2
EF22-DZ-12	221.0	18	193.00	4.32	192.59	3.94	0.26	2	196.62	2.89	3.00	4	195.76	3.11	3.43	195.76	3.11	3.43	193.00	192.59	3.94	0.26	2	204.48	3.10	1.62	4	192.88	5.5
LEF-98	195.1	22	214.08	8.13	503.08	8.24	0.04	2	508.06	7.22	3.02	3	264.50	3.63	128.90	508.06	7.22	3.02	503.20	503.08	8.24	0.04	2	541.31	5.93	1.91	5	214.53	9.8
LEF-79	185.5	54	205.66	6.55	495.65	5.63	0.38	5	504.53	3.26	1.58	13	252.72	4.42	208.32	494.94	6.49	0.45	518.40	503.02	3.49	1.21	12	519.76	2.14	6.44	38	205.79	8.1
LEF-68	171.3	36	195.00	7.76	197.26	2.97	0.17	6	198.01	2.80	0.51	7	196.22	4.19	0.08	196.48	3.88	0.10	197.60	199.40	2.60	1.41	8	198.01	2.80	0.51	7	201.29	3.0
LEF-45	165.5	75	197.22	7.02	201.62	2.92	0.81	5	203.48	2.38	1.15	8	200.72	3.36	1.05	200.72	3.36	1.05	209.80	202.87	2.53	1.02	7	206.77	1.82	2.08	14	205.92	2.7
EF22-DZ-08	163.0	49	193.27	6.71	196.38	4.20	1.44	2	201.53	2.43	1.61	8	197.58	3.70	1.43	198.57	3.47	2.38	203.90	203.35	2.53	0.94	8	205.21	2.08	4.26	12	198.07	3.7
EF22-DZ-07	133.5	12	197.00	5.59	197.38	3.64	0.20	3	197.38	3.64	0.20	3	197.38	3.64	0.20	197.38	3.64	0.20	197.30	197.38	3.64	0.20	3	197.38	3.64	0.20	3	197.43	3.8
EF22-DZ-06	126.3	11	223.00	6.83	280.96	6.35	1.70	2	525.57	6.62	0.83	5	243.49	3.92	57.07	524.16	7.79	1.42	279.00	525.57	6.62	0.83	5	525.57	6.62	0.83	5	222.56	7.4
EF22-DZ-05	111.3	8	217.00	4.75	216.74	4.01	0.05	2	220.17	3.18	3.82	3	220.17	3.18	3.82	220.17	3.18	3.82	216.80	216.74	4.01	0.05	2					216.60	4.6
EF22-DZ-04	69.3	81	190.00	8.66	203.27	4.02	1.06	3	206.36	2.66	1.09	7	198.81	4.29	3.37	203.85	3.80	1.37	216.90	213.46	1.36	1.00	27	215.67	1.09	2.41	47	214.40	1.3
EF22-DZ-02	16.3	47	206.00	5.75	208.29	2.97	0.74	4	211.46	2.24	2.17	7	207.43	3.40	0.61	207.43	3.40	0.61	217.10	208.29	2.97	0.74	4	215.29	1.69	3.57	15	213.66	2.3
LA-ICP-MS (Random)																													
Sample	Thickness	N	YSG	±2σ	YC1s	±2σ	MSWD	N	YC2s	±2σ	MSWD	N	Y3Za	±2σ	MSWD	Y3Zo Ma	±2σ	MSWD	YPP	YSP	±2σ	MSWD	N	tau	±2σ	MSWD	N	MLA	±2σ
EF22-DZ-11	420.55	136	183.33	2.74	184.18	2.23	1.26	2	191.53	1.55	2.39	5	185.01	2.06	2.44	190.66	1.90	3.52	183.80	191.96	2.16	0.72	2	192.46	1.67	0.47	4	183.95	3.4
EF22-DZ-09	361.55	149	196.71	5.71	199.42	2.23	0.48	4	201.28	1.68	1.67	7	198.85	2.59	0.37	198.85	2.59	0.37	200.40	200.01	1.92	0.63	5	201.28	1.68	1.67	7	200.64	2.4
EF22-DZ-14	246.55	111	190.72	3.39	264.37	3.27	0.45	2	268.42	2.43	3.42	5	228.08	2.33	480.03	266.30	2.87	3.13	264.80	264.37	3.27	0.45	2	273.41	3.63	0.04	3	191.15	4.8
EF22-DZ-12	221	140	183.70	2.53	237.59	2.04	0.39	5	238.67	1.78	1.20	6	198.27	1.82	223.22	237.43	2.32	0.71	238.10	238.67	1.78	1.20	6	238.67	1.78	1.20	6	183.99	3.67
LEF-98	195.1	131	217.46	3.53	246.00	3.35	0.74	2	276.73	2.61	3.59	4	232.18	2.40	67.94	275.59	2.93	3.99	246.40	246.00	3.35	0.74	2	281.27	3.14	0.87	3	218.07	5.0
LEF-79	185.5	154	240.45	4.48	239.71	3.87	0.48	2	484.56	4.23	2.47	4	244.52	3.81	107.11	483.13	4.57	2.38	240.10	239.71	3.87	0.48	2	498.69	3.25	1.31	9	240.11	4.9
LEF-68	171.25	153	200.30	3.31	199.71	2.79	0.49	2	202.44	2.09	4.49	3	202.44	2.09	4.49	202.44	2.09	4.49	200.00	199.71	2.79	0.49	2	514.57	3.03	0.57	7	365.64	8.5
LEF-45	165.5	164	240.43	5.48	477.75	6.15	0.11	2	480.67	4.81	1.17	3	277.31	3.34	271.78	480.67	4.81	1.17	478.90	480.67	4.81	1.17	3	480.67	4.81	1.17	3	412.2	14.2
EF22-DZ-07	133.5	133	200.06	5.57	207.81	3.03	0.13	2	205.99	2.65	3.03	3	205.99	2.65	3.03	205.99	2.65	3.03	207.70	207.81	3.03	0.13	2	262.63	2.76	1.53	3	201.44	6.4
EF22-DZ-04	69.25	150	195.94	4.34	202.92	3.90	0.43	2	199.73	2.87	3.03	3	199.73	2.87	3.03	199.73	2.87	3.03	202.70	202.92	3.90	0.43	2	211.40	2.32	0.07	3	196.89	5.4
EF22-DZ-03	18.25	43	222.84	4.33	539.06	3.87	0.20	5	540.77	3.66	1.56	6	235.73	2.30	77.57	539.22	4.27	0.38	539.50	540.77	3.66	1.56	6	539.06	3.87	0.20	5	519.3	16.8
EF22-DZ-02	16.25	160	219.52	4.12	461.43	6.84	0.30	2	467.07	4.13	1.14	5	239.83	2.18	181.02	466.46	4.61	1.30	469.50	467.07	4.13	1.14	5	467.07	4.13	1.14	5	220.9	5.7

CA-ID-TIMS					
Sample	Thickness	N	MDA	±2σ	Method
EF22-DZ-11	420.55	3	194.73	0.07	WMA
EF22-DZ-09	361.55	1	196.94	0.13	YSG
LEF-45	165.5	3	201.64	0.15	WMA
EF22-DZ-08	162	2	201.32	0.10	WMA
EF22-DZ-04	69.25	3	205.47	0.08	WMA
EF22-DZ-02	16.25	2	208.85	0.11	WMA

Table 3.1: Maximum depositional age calculations for samples from Barkley Pass, South Africa.

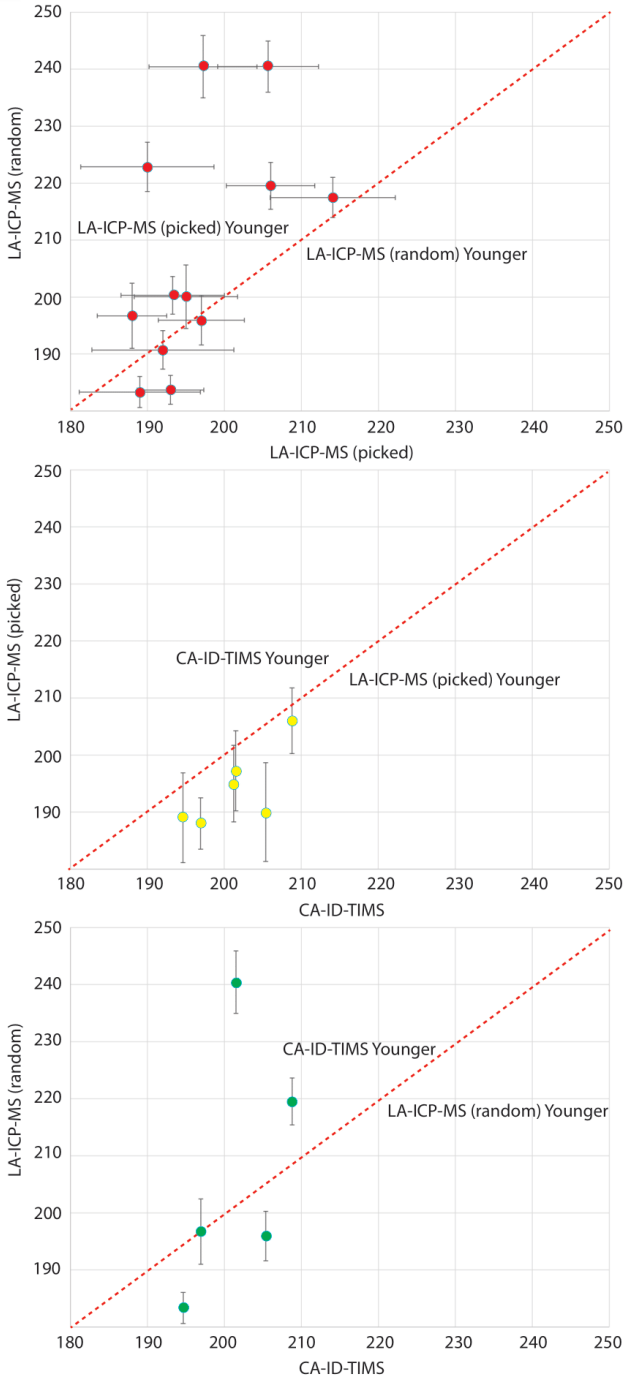

Figure 3.5: Scatterplots showing the degree of agreement between the youngest single grain between (A) random and handpicked separates, (B) handpicked LA-ICP-MS and CA-ID-TIMS, and (C) random LA-ICP-MS and CA-ID-TIMS.

δMDA of Picked VS TIMS									
	YSG	YC1s	YC2s	Y3Za	Y3Zo	YPP	YSP	tau	MLA
EF22-DZ-11	*-2.9403*	-0.6381	0.7385	*-2.2317*	*-1.5283*	0.8086	0.7786	1.6553	0.9781
EF22-DZ-09	*-4.5378*	*-3.7797*	*-2.0592*	*-3.7797*	*-3.7797*	*-1.1865*	*-2.1472*	-0.5402	-0.8768
LEF-45	*-2.1906*	-0.0078	0.9110	-0.4578	-0.4578	4.0469	0.6080	2.5466	2.1227
EF22-DZ-08	*-3.9961*	*-2.4524*	0.1064	*-1.8563*	*-1.3649*	1.2833	1.0093	1.9357	*-1.6127*
EF22-DZ-04	*-7.5271*	*-1.0664*	0.4373	*-3.2399*	-0.7845	5.5651	3.8885	4.9643	4.3484
EF22-DZ-02	*-1.3626*	-0.2683	1.2536	-0.6761	-0.6761	3.9523	-0.2683	3.0845	2.3052
δMDA of Random VS TIMS									
EF22-DZ-11	*-5.8538*	*-5.4166*	*-1.6429*	*-4.9912*	*-2.0876*	*-5.6107*	*-1.4180*	*-1.1619*	*-5.5337*
EF22-DZ-09	-0.1135	1.2595	2.2041	0.9735	0.9735	1.7586	1.5624	2.2041	1.8805
LEF-45	19.2368	136.9301	138.3813	37.5252	138.3813	137.5028	138.3813	138.3813	104.4240
EF22-DZ-04	*-4.6369*	*-1.2393*	*-2.7913*	*-2.7913*	*-2.7913*	*-1.3460*	*-1.2393*	2.8873	*-4.1737*
EF22-DZ-02	5.1123	120.9432	123.6422	14.8342	123.3503	124.8071	123.6422	123.6422	5.7718

Table 3.2: δ_{MDA} of MDA calculation methods when compared to selected CA-ID-TIMS MDA. Offsets that are <-5% are dark red and italic, offsets that are <-1% and >-5% are light red and italic. Offsets that are within ±1% of the CA-ID-TIMS MDA are green, and offsets >1% are colored gray.

Discussion

Accuracy of LA-ICP-MS MDA calculations relative to CA-ID-TIMS

How well do MDAs calculated from LA-ICP-MS data agree with the higher resolution and more accurate CA-ID-TIMS results? Often, authors will calculate MDAs with LA-ICP-MS dates alone. This study serves the dual purpose of constraining the age of a geologically significant formation and assessing the use of LA-ICP-MS MDAs compared to CA-ID-TIMS. The new zircon U-Pb data from this study constrains the MDA of the Elliot formation from 208.80 ± 0.14 Ma (EF22-DZ-02; 16.25 m above the base of the section) to 194.65 ± 0.13 Ma (EF22-DZ-11; 5 m below the top of the Elliot Formation). Following Schwartz et al. (2023), I compared all nine MDA calculation methods from random and handpicked aliquots to CA-ID-TIMS (Table 3.2).

For MDAs based on the handpicked LA-ICP-MS data, 35% of all comparisons were within 1% of the CA-ID-TIMS MDA. In comparison, 7% of all MDAs based on random LA-ICP-MS data were within 1% of the CA-ID-TIMS MDA (Table 3.2). Authors will pick though zircon separates in order to date the most euhedral zircon which have undergone the least transportation (Fralick et al., 2002; Markwitz et al., 2017; Bullard, 2018; Žák and Sláma, 2018; Fekete et al., 2023). Multiple studies, including this one, speculate that picking of sharp euhedral zircon and dating them will aid in analyzing younger dates that can be used for more accurate MDA calculations (Herriott et al., 2019; Dröllner et al., 2021; Fekete et al., 2023). Evidence shows that an MDA calculation's performance relative to CA-ID-TIMS is variable between samples and methods. Random aliquots' MDA calculation accuracy relative to CA-ID-TIMS are more dependent on sample, and handpicked aliquots' MDA calculation is more dependent on the MDA calculation method. For example, for samples LEF-45 and EF22-DZ-11, five of the nine handpicked aliquot MDA calculation methods are within 1% of CA-ID-TIMS analyses. However, neither LEF-45 nor EF22-DZ-11 have a single MDA calculation method from a random aliquot that is within 1% of the CA-ID-TIMS MDA (Table 3.2). Only sample EF22-DZ-09 has random aliquot MDAs that are within 1% of the CA-ID-TIMS MDA, likely because EF22-DZ-09 has the most near depositional zircon of any random aliquot (16%) (Fig. 3.4). Handpicked aliquots regularly produced more near depositional grains and more accurate MDAs in comparison to random aliquots (Table 3.2).

MDA calculations from the handpicked LA-ICP-MS data are regularly inconsistent with CA-ID-TIMS results. However, some calculations perform better than others. The YSG for handpicked samples gave a younger MDA than that of CA-ID-TIMS for every sample (Fig. 3.2). YC1σ, Y3Za, and Y3Zo all produce MDAs that are younger than the CA-ID-TIMS date, but these

calculation methods also have varying degrees of success when it comes to agreement with CA-ID-TIMS (Table 3.2). YPP and the τ method regularly produce MDAs that are older than the CA-ID-TIMS MDA with one exception being from sample EF22-DZ-09 which has the highest proportion of near depositional grains (75%) (Fig. 3.4). YSP and MLA were within 1% of the CA-ID-TIMS date twice and once respectively, they both regularly had MDAs that were older than that of CA-ID-TIMS MDAs. YC1σ, Y3zo, and YSP are all tied for the second-best performing MDA calculation of all methods (three of six samples within 1% of CA-ID-TIMS date). The best performing MDA calculation method compared to CA-ID-TIMS is YC2σ; four of the six samples had an MDA within 1% of the CA-ID-TIMS MDA (Table 3.2). Other authors have a preference for MDA calculations that are more "statistically sound" than that of YC2σ (Vermeesch, 2021; Schwartz et al., 2023), and others prefer a less conservative method of calculation (Copeland, 2020a). It has been noted by authors that dating zircon with CA-ID-TIMS after LA-ICP-MS can improve the precision and accuracy of MDA calculations (Bullard, 2018; Herriott et al., 2019; Dehler et al., 2023). For this study, and from my comparison of handpicked aliquots to CA-ID-TIMS MDAs, YC2σ is my preferred method of MDA calculation when CA-ID-TIMS is unavailable.

Handpicked aliquots' MDAs regularly overlap within 2 sigma uncertainty of CA-ID-TIMS MDAs (Fig. 3.6.). It is easily observed in Figure 3.6 that some MDA methods tend to be older or younger than CA-ID-TIMS MDAs, where my six samples dated with CA-ID-TIMS are compared to LA-ICP-MS MDAs. Of the mentioned six samples, all have a handpicked LA-ICP-MS YSG that are younger than its CA-ID-TIMS MDA. The YSG from random aliquots are less likely to be younger than that of CA-ID-TIMS (Table 3.2). However, there are fewer YSGs in random analyses that are near depositional age. In some cases, the YSG of a random aliquot may be 20% older than

that of the CA-ID-TIMS YSG (Table 3.2). Even after accounting for uncertainty, only one YSG from a random aliquot (sample EF22-DZ-09) is within uncertainty of the sample's CA-ID-TIMS MDA (Table 3.1).

It has been noted that the youngest grain of any dataset is all that is needed to interpret the MDA of a sediment, to avoid unnecessary and inappropriate averaging of data (Copeland, 2020). However, the previous notion does not account for the understanding that Pb loss is promoted in low temperatures which are common in sedimentary basin settings, where all zircon can be affected (Cherniak and Watson, 2001; Schoene, 2013; Vermeesch, 2021). However, in handpicked aliquots, all YSGs are younger than the corresponding CA-ID-TIMS data, and are interpreted to be a poor estimate of the MDA because of unmitigated Pb loss (Black, 1987; Von Quadt et al., 2014; Coutts et al., 2019; Keller et al., 2019; Sharman and Malkowski, 2020; Gehrels et al., 2020). Copeland (2020) argues that only post-depositional Pb loss poses a problem to MDA. However, post-depositional Pb loss is implied in datasets where the YSG measured via LA-ICP-MS is younger than the depositional age, including in this study (Schoene, 2013; Andersen et al., 2019; Sharman and Malkowski, 2023).

Constraining the Age of the Elliot Formation

Previous work done by Bordy et al. (2020) has constrained the MDA of the lowermost and uppermost Elliot Formation to 219.6 Ma and 191.9 Ma, respectively. The MDA from the stratigraphically lowest sample analyzed in this study is 10.8 Myr younger than the oldest MDA reported by Bordy et al. (2020). However, my lowermost sample was ~16 m above the base of the Elliot Formation exposures at Barkley Pass and thus does not capture the base of the formation. Based on regional mapping, the contact between the Molteno and Elliot formations is likely ~10 m below the start of our section.

For the purposes of quantifying sedimentation rate, I assumed that the MDA approximates the true depositional age of each sample. The total thickness of the Elliot Formation at Barkley Pass is 460 m (Bordy and Eriksson, 2015). My lowermost sample EF22-DZ-02 is 16.25 m (Fig. 3.2) from the base of the measured section and is ≤208.80 ± 0.14 Ma. The next CA-ID-TIMS date in the section is from EF22-DZ-04 (69.25 m from the base) and is ≤205.38 ± 0.16 Ma, resulting in an apparent sedimentation rate between these two points of ~15.49 m/Myr. Continuing up section, EF22-DZ-08 (162 m from the base) has a CA-ID-TIMS MDA of 201.23 ± 0.14 Ma suggesting that the apparent sedimentation rate then increased between samples EF22-DZ-04 and -08 to 22.34 m/Myr (Fig. 3.5). The ETE (201.564 ± 0.015 Ma) and the TJB (201.464 ± 0.004 Ma) are interpreted to have occurred between samples EF22-DZ-04 (205.47 ± 0.08 Ma) and -08 (201.32 ± 0.10 Ma) in the Elliot Formation, which are between 82 m and 162 m from the base of section, respectively (Blackburn et al., 2013). High resolution C-isotope ($\delta^{13}C_{org}$) data was collected at Barkley Pass by PhD candidate Danielle Oberg in tandem with this study. $\delta^{13}C_{org}$ values range from ~-20‰ to ~-30‰ with an average of -25.11‰. A major negative excursion of $\delta^{13}C_{org}$ occurs at 154 m is followed by a slight reversal between 159 m and 164 m (Fig. 3.2) (Oberg, 2023). The excursion interpreted to be the ETE is located below EF22-DZ-08, which is consistent with an MDA of 201.32 ± 0.10 Ma (Rhaetian). CAMP volcanism (201.566-200.916 Ma; Blackburn et al., 2013) is interpreted to have driven the negative $\delta^{13}C_{org}$ excursion at 154 m, as a negative $\delta^{13}C_{org}$ excursion has the possibility of being a signature of a large magmatic province (Beerling and Berner, 2002). LEF-45 yielded a slightly older CA-ID-TIMS date (201.64 ± 0.15 Ma) than the underlying sample (EF22-DZ-08; 201.32 ± 0.10 Ma), so it is not useful for sedimentation rate analysis (Fig. 3.3). Sample LEF-45 illustrates the drawback to assuming that the MDA is exactly equal to the true depositional age. EF22-DZ-09 yielded a CA-ID-TIMS MDA of 196.94 ± 0.13 Ma

at 361.55 m from the base of the section (Figs. 3.3 and 3.6), more than doubling the apparent sedimentation rate to 46.51 m/Myr. My uppermost sample, EF22-DZ-11, is 420.55 m from the base and is dated to 194.73 ± 0.07 Ma from a weighted average of the youngest three zircon, lowering the sedimentation rate to 25.7 m/Myr (Figs. 3.2, 3.3, & 3.6).

Previous interpretations of the age of the Elliot Formation have estimated deposition to range from Triassic (Norian) to Jurassic (Sinemurian) in age (~220-191 Ma) (Bordy and Eriksson, 2015, McPhee et al., 2017, Tolchard et al., 2019, Bordy et al., 2020). Additionally, it was thought that the TJB was encompassed within an unconformity at the LEF-UEF boundary, and the ETE slightly below it (Bordy and Catuneanu, 2001; Bordy et al., 2004a; Bordy, 2004; Bordy and Head, 2018). The detrital zircon U-Pb data presented herein supports the established interpretations of the depositional time frame of the Elliot Formation but does not agree with the previously interpreted location of the TJB or ETE in the stratigraphy. My data, and the data of PhD candidate Danielle Oberg, support the idea that the location of the onset of the ETE at the Barkley Pass outcrop is at ~154 m from that base of the section (36 m below the LEF-UEF contact) and the TJB is at ~164 m from the base of the section (36 m below the LEF-UEF contact), well within the uppermost LEF (Oberg, 2023). The previously mentioned constraint will assist in the accuracy of assigning biota to their respective depositional period.

Bordy et al. (2020) presented detrital zircon samples along a north-south transect of the western outcropping range of the Elliot Formation. Furthermore, samples were taken from a wide range of stratigraphic heights at different sections, and no section had more than 4 samples taken from it (Bordy et al., 2020). Bordy et al. (2020)'s sampling in the LEF often targeted the uppermost LEF, which is where the ETE and TJB were expected to be contemporaneous with deposition of the Elliot Formation. Only one CA-ID-TIMS date was taken from the northern margin of the Elliot

Formation in UEF and resulted in an MDA of 202.33 ± 0.19 Ma. From my data, it is now known that at Barkley Pass the Elliot Formation is Jurassic in age (younger than 201.3 Ma; Walker et al., 2013) in the uppermost LEF (Bordy et al., 2020).

Detrital zircon ages determined by random LA-ICP-MS alone have proven difficult to pinpoint the exact stratigraphic position of the ETE and TJB in the Elliot Formation, likely due to relatively high analytical uncertainty (~1.9% at 2σ uncertainty) (Gehrels, 2014). It is noted that in many other studies constraining the MDA of the ETE and TJB, high precision CA-ID-TIMS analyses are preferred even when they are unavailable (Schaltegger et al., 2008; Blackburn et al., 2013; Boudreaux, 2019). Additionally, the Elliot Formation can serve as a complimentary Gondwanan example to the Moenave Formation for studies that aim to understand more about the climate of the ancient Earth.

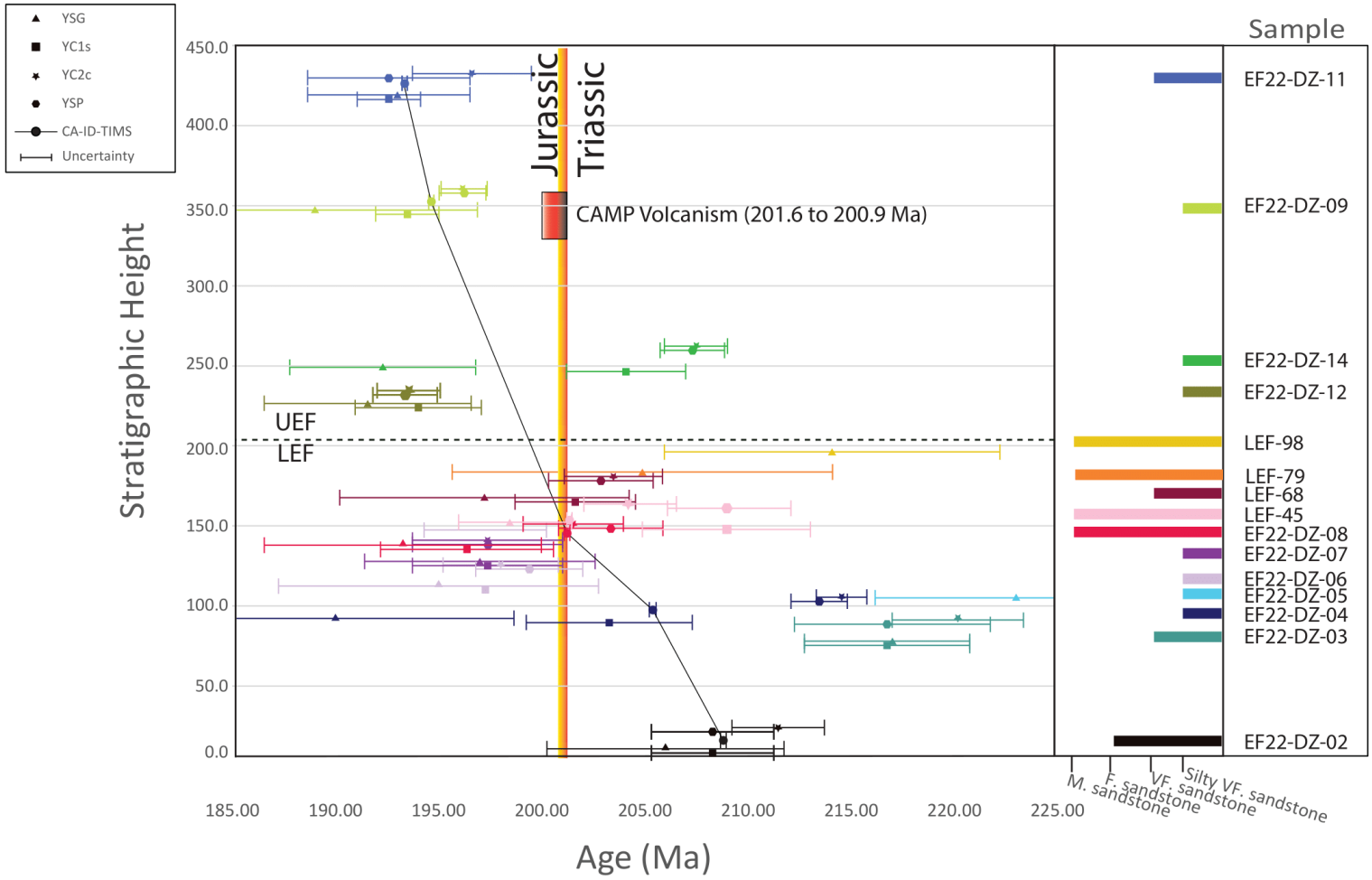

Figure 3.6: Age model for the Elliot Formation at Barkley Pass. Shown are 4 MDA calculation methods (YSG, YC1σ, YC2σ, YSP) based on the LA-ICP-MS data along with the preferred CA-ID-TIMS MDA.

Conclusions

I have demonstrated that samples that have been handpicked for sharp and euhedral facies produce more near-depositional dates than samples that are randomly analyzed. A more accurate MDA can be produced and used for age calculations from handpicked aliquots. For samples that have CA-ID-TIMS analyses, a weighted mean average is my most preferred MDA calculation. However, where CA-ID-TIMS is unavailable, my preferred MDA calculation is YC2σ from LA-ICP-MS analyses.

Historically, lower units in the Karoo Basin (Ecca and Beaufort Groups) have had extensive detrital zircon U-Pb geochronology data gathered from them, due to their prevalence as analogs for offshore/nearshore systems (Lanci et al., 2013; Rubidge et al., 2013; McKay et al. 2015; Viglietti et al., 2018). Previous works had constrained the Elliot Formation's MDA to <219.6 Ma using LA-ICP-MS (Bordy et al., 2020). The Elliot Formation in South Africa and Lesotho has been chronostratigraphically constrained with an MDA of 208.85 ± 0.11 Ma for my stratigraphically lowest sample and 194.73 ± 0.07 Ma for my uppermost sample. With the tandem work being conducted by PhD candidate Danielle Oberg, I have constrained the ETE, the TJB, and CAMP volcanism to the uppermost LEF at Barkley. From handpicked samples and CA-ID-TIMS analyses I have calculated an approximate average sedimentation rate of ~27.2 m/Myr at Barkley Pass. MDAs from this study will likely be used in future studies to numerically constrain taxon ranges of biostratigraphically significant organisms in the Elliot Formation.

References

Allen, C.M., and Campbell, I.H., 2012, Identification and elimination of a matrix-induced systematic error in LA–ICP–MS $^{206}Pb/^{238}U$ dating of zircon: Chemical Geology, v. 332–333, p. 157–165, doi:10.1016/j.chemgeo.2012.09.038.

Andersen, T., Elburg, M.A., and Magwaza, B.N., 2019, Sources of bias in detrital zircon geochronology: Discordance, concealed lead loss and common lead correction: Earth-Science Reviews, v. 197, doi:10.1016/j.earscirev.2019.102899.

Barrett, P.M., Botha, J., Chapelle, K., Staunton, C.K., and Choiniere, J., 2019, Postcranial osteology of the neotype specimen of Massospondylus carinatus Owen, 1854 (Dinosauria: Sauropodomorpha) from the upper Elliot formation of South Africa Dental evolution in gomphodont cynodonts Palaeontologia Africana, v. 53, p. 114-178

Beerling, D.J., and Berner, R.A., 2002, Biogeochemical constraints on the Triassic-Jurassic boundary carbon cycle event: Global Biogeochemical Cycles, Palaeontologia Africana, v. 16, doi:10.1029/2001GB001637.

Black, L.P., Kamo S.L., Allen, C.M. Davis, D.W., Aleinikoff J.N., Valley, J.W. Mundil, R., campbell, I.H., Korsch, R.J., Williams, I.S., foudoulis, C., 2004, Improved $^{206}Pb/^{238}U$ microprobe geochronology by the monitoring of a trace-element-related matrix effect; SHRIMP, ID–TIMS, ELA–ICP–MS and oxygen isotope documentation for a series of zircon standards: Chemical Geology, v. 205, p. 115–140, doi:10.1016/j.chemgeo.2004.01.003.

Black, L.P., 1987, Recent Pb loss in zircon: A natural or laboratory-induced phenomenon? Chemical Geology: Isotope Geoscience section, v. 65, p. 25–33, doi:10.1016/0168-9622(87)90059-5.

Blackburn, T.J., Paul, E.O., Bowring, S.A., Mclean, N.M., Kent, D.V., Puffer, J., Mchone, G., Rasbury, E.T., and Et-Touhami, M., 2013, Zircon U-Pb Geochronology Links the End-Triassic Extinction with the Central Atlantic Magmatic Province v. 340, p. 941-945, doi:10.1126/science.1234204.

Bordy, E.M. et al., 2020, A chronostratigraphic framework for the upper Stormberg Group: Implications for the Triassic-Jurassic boundary in southern Africa: Earth-Science Reviews, v. 203, p. 103-120, doi:10.1016/j.earscirev.2020.103120.

Bordy, E.M., 2004, Basin development during the deposition of the Elliot Formation (Late Triassic - Early Jurassic), Karoo Supergroup, South Africa: South African Journal of Geology, v. 107, p. 397–412, doi:10.2113/107.3.397.

Bordy, E.M., and Abrahams, M., 2016, Geochemistry of the Pronksberg Bentonite of the Upper Elliot Formation (Early Jurassic), Eastern Cape, South Africa, *in* Linol, B. and De Wit, M.J. eds., Origin and Evolution of the Cape Mountains and Karoo Basin, Cham, Springer International Publishing, Regional Geology Reviews, p. 119–127, doi:10.1007/978-3-319-40859-0_12.

Bordy, E.M., and Catuneanu, O., 2001, Sedimentology of the upper Karoo fluvial strata in the Tuli Basin, South Africa:, Journal of African Earth Sciences, v. 33, p. 605-629, doi:10.1016/S0899-5362(01)00090-2.

Bordy, E.M., and Eriksson, P., 2015, Lithostratigraphy of the Elliot Formation (Karoo Supergroup), South Africa: South African Journal of Geology, v. 118, p. 311–316, doi:10.2113/gssajg.118.3.311.

Bordy, E.M., Hancox, P.J., and Rubidge, B.S., 2004a, A description of the sedimentology and palaeontology of the Late Triassic–Early Jurassic Elliot formation in Lesotho: Palaeontologia Africana, v. 40, p. 45–60.

Bordy, E.M., Hancox, P.J., and Rubidge, B.S., 2004b, Provenance study of the Late Triassic - Early Jurassic Elliot Formation, main Karoo Basin, South Africa: South African Journal of Geology, v. 107, p. 587–602, doi:10.2113/gssajg.107.4.587.

Bordy, E.M., and Head, H.V., 2018, Lithostratigraphy of the Clarens Formation (Stormberg Group, Karoo Supergroup), South Africa: South African Journal of Geology, v. 121, p. 119–130, doi:10.25131/sajg.121.0009.

Bordy, E.M., Sciscio, L., Abdala, F., McPhee, B.W., and Choiniere, J.N., 2017, First Lower Jurassic vertebrate burrow from southern Africa (upper Elliot Formation, Karoo Basin, South Africa): Palaeogeography, Palaeoclimatology, Palaeoecology, v. 468, p. 362–372, doi:10.1016/j.palaeo.2016.12.024.

Boudreaux, A.R., 2019, Provenance and Maximum Depositional Age Analysis of the Moenave Formation using Detrital Zircon U-Pb Geochronology and Sandstone Petrography [MS Thesis]: University of Arkansas, 71 p.

Bowden, L.L., 2014, A comparative study of detrital zircon ages from river sediment and rocks of the Karoo Supergroup (Late Carboniferous to Jurassic), Eastern Cape Province, South Africa: implications for the tectono-sedimentary evolution of Gondwanaland's southern continental margin [PhD Thesis]: University of Johannesburg, 30 p.

Bullard, A., 2018, New CA-ID-TIMS detrital zircon constraints on middle Neoproterozoic sedimentary successions, southwestern United States [MS Thesis]: Utah State University, 70 p., doi:10.26076/21c8-0a92

Chapelle, K.E.J., Barrett, P.M., Botha, J., and Choiniere, J.N., 2019, Ngwevu intloko: A new early sauropodomorph dinosaur from the Lower Jurassic Elliot Formation of South Africa and comments on cranial ontogeny in Massospondylus carinatus: PeerJ, v. 7, doi:10.7717/peerj.7240.

Cherniak, D.J., and Watson, E.B., 2001, Pb diffusion in zircon: Chemical Geology, v. 172, p. 5–24, doi:10.1016/S0009-2541(00)00233-3.

Copeland, P., 2020, On the use of geochronology of detrital grains in determining the time of deposition of clastic sedimentary strata: Basin Research, v. 32, p. 1532–1546, doi:10.1111/bre.12441.

Corfu, F., 2013, A century of U-Pb geochronology: The long quest towards concordance: Geological Society of America Bulletin, v. 125, p. 33–47, doi:10.1130/B30698.1.

Cottle, J.M., Horstwood, M.S.A., and Parrish, R.R., 2009, A new approach to single shot laser ablation analysis and its application to in situ Pb/U geochronology: Journal of Analytical Atomic Spectrometry, v. 24, p. 13-55, doi:10.1039/b821899d.

Cottle, J.M., Kylander-Clark, A.R., and Vrijmoed, J.C., 2012, U–Th/Pb geochronology of detrital zircon and monazite by single shot laser ablation inductively coupled plasma mass spectrometry (SS-LA-ICPMS): Chemical Geology, v. 332–333, p. 136–147, doi:10.1016/j.chemgeo.2012.09.035.

Coutts, D.S., Matthews, W.A., and Hubbard, S.M., 2019, Assessment of widely used methods to derive depositional ages from detrital zircon populations: Geoscience Frontiers, v. 10, p. 1421–1435, doi:10.1016/j.gsf.2018.11.002.

Cox, G.M. et al., 2018, South Australian U-Pb zircon (CA-ID-TIMS) age supports globally synchronous Sturtian deglaciation: Precambrian Research, v. 315, p. 257–263, doi:10.1016/j.precamres.2018.07.007.

Crowley, Q.G., Heron, K., Riggs, N., Kamber, B., Chew, D., McConnell, B., and Benn, K., 2014, Chemical abrasion applied to LA-ICP-MS U–Pb zircon geochronology: Minerals, v. 4, p. 503–518, doi:10.3390/min4020503.

Davis, D.W., Williams, I.S., and Krogh, T.E. 6 Historical, 2003, Development of Zircon Geochronology: Reviews in Mineralogy and Geochemistry, v. 53, p. 145-181, doi: 10.2113/0530145

Dehler, C., Schmitz, M., Bullard, A., Porter, S., Timmons, M., Karlstrom, K., and Cothren, H., 2023, Precise U-Pb age models refine Neoproterozoic western Laurentian rift initiation, correlation, and Earth system changes: Precambrian Research, v. 396, p. 107-156, doi:10.1016/j.precamres.2023.107156.

Dickin, A.P., 1995, Radiogenic Isotope Geology: Cambridge University Press, v. 3, p. 180–195, doi:10.1017/S0016756800008852

Donaghy, E.E., Eddy, M.P., Moreno, F., and Ibañez-Mejia, M., 2023, Increased accuracy and precision in igneous and detrital zircon geochronology using CA-LA-ICPMS: Geochronological data analysis/statistics/modelling preprint, doi:10.5194/gchron-2023-20.

Dröllner, M., Barham, M., and Kirkland, C.L., 2022, Gaining from loss: Detrital zircon source-normalized α-dose discriminates first-versus multi-cycle grain histories: Earth and Planetary Science Letters, v. 579, doi:10.1016/j.epsl.2021.117346.

Dröllner, M., Barham, M., Kirkland, C.L., and Ware, B., 2021, Every zircon deserves a date: selection bias in detrital geochronology: Geological Magazine, v. 158, p. 1135–1142, doi:10.1017/S0016756821000145.

Eggins, S.M., Kinsley, L.P.J., and Shelley, J.M.G., 1998, Deposition and element fractionation processes during atmospheric pressure laser sampling for analysis by ICP-MS: Applied Surface Science, v. 127–129, p. 278–286, doi:10.1016/S0169-4332(97)00643-0.

Ellis, B.S., Schmitz, M.D., and Hill, M., 2019, Reconstructing a Snake River Plain 'super-eruption' via compositional fingerprinting and high-precision U/Pb zircon geochronology: Contributions to Mineralogy and Petrology, v. 174, p. 101, doi:10.1007/s00410-019-1641-z.

Fekete, J., Sharman, G.R., Crowley, J.L., and Howard, B., 2023, Leaving No Zircon Unturned: Quantifying the Impact of Handpicking vs Random Analysis of Detrital Zircon On Maximum Depositional Age Analysis, GSA Connects 2023 in Pittsburgh, PA, USA, Geological Society of America, abstract 20-11.

Finzel, E.S., and Rosenblume, J.A., 2021, Dating lacustrine carbonate strata with detrital zircon U-Pb geochronology: Geology, v. 49, p. 294–298, doi:10.1130/G48070.1.

Fralick, P., Davis, D.W., and Kissin, S.A., 2002, The age of the Gunflint Formation, Ontario, Canada: single zircon UPb age determinations from reworked volcanic ash: Canadian Journal of Earth Sciences, v. 39, p. 1085–1091, doi:10.1139/e02-028.

Gardner, C.T., Finzel, E.S., Rosenblume, J.A., and Pearson, D.M., 2022, Foreland basin response to middle Cretaceous thrust belt evolution, southwestern Montana, USA: Geosphere, v. 18, p. 1783–1803, doi:10.1130/GES02521.1.

Gaschnig, R.M., Vervoort, J.D., Lewis, R.S., and McClelland, W.C., 2010, Migrating magmatism in the northern US Cordillera: in situ U–Pb geochronology of the Idaho batholith: Contributions to Mineralogy and Petrology, v. 159, p. 863–883, doi:10.1007/s00410-009-0459-5.

Gehrels, G., 2014, Detrital zircon U-Pb geochronology applied to tectonics: Annual Review of Earth and Planetary Sciences, v. 42, p. 127–149, doi:10.1146/annurev-earth-050212-124012.

Gehrels, G. et al., 2020, LA-ICPMS U–Pb geochronology of detrital zircon grains from the Coconino, Moenkopi, and Chinle formations in the Petrified Forest National Park (Arizona): Geochronology, v. 2, p. 257–282, doi:10.5194/gchron-2-257-2020.

Giles, K.D., Jackson, W.T., McKay, M.P., Beebe, D.A., Larsen, D., Kwon, Y., and Shaulis, B., 2023, Sediment input, alongshore transport, and coastal mixing in the northeastern Gulf of Mexico based on detrital-zircon geochronology: Marine and Petroleum Geology, v. 148, p. 105997, doi:10.1016/j.marpetgeo.2022.105997.

Ginster, U., Reiners, P.W., Nasdala, L., and N, C.C., 2019, Annealing kinetics of radiation damage in zircon: Geochimica et Cosmochimica Acta, v. 249, p. 225–246, doi:10.1016/j.gca.2019.01.033.

Hanchar, J.M., and Miller, C.F., 1993, Zircon zonation patterns as revealed by cathodoluminescence and backscattered electron images: Implications for interpretation of complex crustal histories: Chemical Geology, v. 110, p. 1–13, doi:10.1016/0009-2541(93)90244-D.

Hao, H., Campbell, I.H., Cooke, D.R., Nakamura, E., and Sakaguchi, C., 2021, Geochronology, Petrogenesis and Oxidation State of the Northparkes Igneous Suite, New South Wales, Australia: Implications for Magma Fertility: Economic Geology, v. 116, p. 1161–1187, doi:10.5382/econgeo.4825.

Herriott, T.M., Crowley, J.L., Schmitz, M.D., Wartes, M.A., and Gillis, R.J., 2019, Exploring the law of detrital zircon: LA-ICP-MS and CA-TIMS geochronology of Jurassic forearc strata, Cook Inlet, Alaska, USA: Geology, v. 47, p. 1044–1048, doi:10.1130/G46312.1.

Johnston, S., Gehrels, G., Valencia, V., and Ruiz, J., 2009, Small-volume U–Pb zircon geochronology by laser ablation-multicollector-ICP-MS: Chemical Geology, v. 259, p. 218–229, doi:10.1016/j.chemgeo.2008.11.004.

Keeley, J.A., Link, P.K., Fanning, C.M., and Schmitz, M.D., 2013, Pre- to synglacial rift-related volcanism in the Neoproterozoic (Cryogenian) Pocatello Formation, SE Idaho: New SHRIMP and CA-ID-TIMS constraints: Lithosphere, v. 5, p. 128–150, doi:10.1130/L226.1.

Keller, C., Boehnke, P., Schoene, B., and Harrison, T.M., 2019, Stepwise chemical abrasion–isotope dilution–thermal ionization mass spectrometry with trace element analysis of microfractured Hadean zircon: Geochronology, v. 1, p. 85–97, doi:10.5194/gchron-1-85-2019.

Lanci, L., Tohver, E., Wilson, A., and Flint, S., 2013, Upper Permian magnetic stratigraphy of the lower Beaufort Group, Karoo Basin: Earth and Planetary Science Letters, v. 375, p. 123–134, doi:10.1016/j.epsl.2013.05.017.

Marillo-Sialer, E., Woodhead, J., Hanchar, J.M., Reddy, S.M., Greig, A., Hergt, J., and Kohn, B., 2016, An investigation of the laser-induced zircon 'matrix effect': Chemical Geology, v. 438, p. 11–24, doi:10.1016/j.chemgeo.2016.05.014.

Markwitz, V., Kirkland, C.L., Mehnert, A., Gessner, K., and Shaw, J., 2017, 3-D Characterization of Detrital Zircon Grains and its Implications for Fluvial Transport, Mixing, and Preservation Bias: Geochemistry, Geophysics, Geosystems, v. 18, p. 4655–4673, doi:10.1002/2017GC007278.

Mattinson, J.M., 2010, Analysis of the relative decay constants of ^{235}U and ^{238}U by multi-step CA-TIMS measurements of closed-system natural zircon samples: Chemical Geology, v. 275, p. 186–198, doi:10.1016/j.chemgeo.2010.05.007.

Mattinson, J.M., 2005, Zircon U–Pb chemical abrasion ("CA-TIMS") method: Combined annealing and multi-step partial dissolution analysis for improved precision and accuracy of zircon ages: Chemical Geology, v. 220, p. 47–66, doi:10.1016/j.chemgeo.2005.03.011.

McKanna, A.J., Koran, I., Schoene, B., and Ketcham, R.A., 2023, Chemical abrasion: the mechanics of zircon dissolution: Geochronology, v. 5, p. 127–151, doi:10.5194/gchron-5-127-2023.

McKay, M.P., Weislogel, A.L., Fildani, A., Brunt, R.L., Hodgson, D.M., and Flint, S.S., 2015, U-Pb zircon tuff geochronology from the Karoo Basin, South Africa: Implications of zircon recycling on stratigraphic age controls: International Geology Review, v. 57, p. 393–410, doi:10.1080/00206814.2015.1008592.

McPhee, B.W., Bordy, E.M., Sciscio, L., and Choiniere, J.N., 2017, The sauropodomorph biostratigraphy of the Elliot Formation of southern Africa: Tracking the evolution of sauropodomorpha across the Triassic-Jurassic boundary: Acta Palaeontologica Polonica, v. 62, p. 441–465, doi:10.4202/app.00377.2017.

McPhee, B.W., and Choiniere, J.N., 2016, A hyper-robust sauropodomorph dinosaur ilium from the Upper Triassic–Lower Jurassic Elliot Formation of South Africa: Implications for the functional diversity of basal Sauropodomorpha: Journal of African Earth Sciences, v. 123, p. 177–184, doi:10.1016/j.jafrearsci.2016.08.004.

Mmasa, D., 2021, Effects of the Triassic-Jurassic Central Atlantic Magmatic Event Recorded in Continental Strata in Western Pangea: The δ13C Record of Warner Valley & Zion National Park [MS Thesis]: University of Arkansas, 96 p.

Morales, I., Molina, J.F., Montero, P., Bea, F., and Cambeses, A., 2022, Annealing experiments on zircons: influence of lattice orientation and metamictization, EGU General Assembly 2022 in Vienna, Austria, European Geophysical Union, abstract EGU22-1195.

Murakami, T., Chakoumakos, B.C., Ewing, R.C., Lumpkin, G.R., and Weber, W.J., 1991, Alpha-decay event damage in zircon: American Mineralogist, v. 76, p. 1510–1532.

Niemi, N., 2013, Detrital zircon age distributions as a discriminator of tectonic versus fluvial transport: An example from the Death Valley, USA, extended terrane: Geosphere, v. 9, p. 126, doi:10.1130/GES00820.1.

Oberg, D., 2023, C-Isotope Chemostratigraphy of The Elliot Formation of Southern Africa, GSA Connects 2023 in Pittsburgh, PA, USA, Geological Society of America, abstract 254-8.

Oefinger, J., 2021, Carbon-Isotope Chemostratigraphy and Fluvial Sedimentology of the Moenave Formation, Utah [MS Thesis]: University of Arkansas, 69 p.

Olierook, H.K.H. et al., 2021, Regional zircon U-Pb geochronology for the Maniitsoq region, southwest Greenland: Scientific Data, v. 8, p. 139, doi:10.1038/s41597-021-00922-x.

Olsen, P.E., and Galton, P.M., 1984, A review of the reptile and amphibian assemblages from the Stormberg Group of southern Africa with special emphasis on the footprints and the age of the Stormberg: Palaeontologia Africana, v. 25, p. 87–110

Puetz, S.J., 2018, A relational database of global U–Pb ages: Geoscience Frontiers, v. 9, p. 877–891, doi:10.1016/j.gsf.2017.12.004.

Rasmussen, C. et al., 2020, U-Pb zircon geochronology and depositional age models for the Upper Triassic Chinle Formation (Petrified Forest National Park, Arizona, USA): implications for Late Triassic paleoecological and paleoenvironmental change: GSA Bulletin, v.133, p. 539-558, doi:10.7916/D8-K9R9-S495.

Rivera, T.A., Schmitz, M.D., Jicha, B.R., and Crowley, J.L., 2016, Zircon Petrochronology and $^{40}Ar/^{39}Ar$ Sanidine Dates for the Mesa Falls Tuff: Crystal-scale Records of Magmatic Evolution and the Short Lifespan of a Large Yellowstone Magma Chamber: Journal of Petrology, v. 57, p.1677-1704, doi:10.1093/petrology/egw053.

Rubidge, B.S., Erwin, D.H., Ramezani, J., Bowring, S.A., and Klerk, W.J. de, 2013, High-precision temporal calibration of Late Permian vertebrate biostratigraphy: U-Pb zircon constraints from the Karoo Supergroup, South Africa: Geology, v. 41, p. 363–366, doi:10.1130/G33622.1.

Schaltegger, U., Guex, J., Bartolini, A., Schoene, B., and Ovtcharova, M., 2008, Precise U–Pb age constraints for end-Triassic mass extinction, its correlation to volcanism and Hettangian post-extinction recovery: Earth and Planetary Science Letters, v. 267, p. 266–275, doi:10.1016/j.epsl.2007.11.031.

Schaltegger, U., Schmitt, A.K., and Horstwood, M.S.A., 2015, U–Th–Pb zircon geochronology by ID-TIMS, SIMS, and laser ablation ICP-MS: Recipes, interpretations, and opportunities: Chemical Geology, v. 402, p. 89–110, doi:10.1016/j.chemgeo.2015.02.028.

Schoene, B., 2013, U-Th-Pb Geochronology, in Treatise on Geochemistry: Second Edition, Elsevier Inc., v. 4, p. 341–378, doi:10.1016/B978-0-08-095975-7.00310-7.

Schoene, B., Condon, D.J., Morgan, L., and McLean, N., 2013b, Precision and Accuracy in Geochronology: Elements, v. 9, p. 19–24, doi:10.2113/gselements.9.1.19.

Schwartz, T.M., Souders, A.K., Lundstern, J.-E., Gilmer, A.K., and Thompson, R.A., 2023, Revised age and regional correlations of Cenozoic strata on Bat Mountain, Death Valley region, California, USA, from zircon U-Pb geochronology of sandstones and ash-fall tuffs: Geosphere, v. 19, p. 235–257, doi:10.1130/GES02543.1.

Sciscio, L., Kock, M. de, Bordy, E., and Knoll, F., 2017, Magnetostratigraphy across the Triassic-Jurassic boundary in the main Karoo Basin: Gondwana Research, v. 51, p. 177–192, doi:10.1016/j.gr.2017.07.009.

Sharman, G.R., and Malkowski, M.A., 2023, Modeling apparent Pb loss in zircon U-Pb geochronology: Geochronological data analysis/statistics/modelling preprint, doi:10.5194/gchron-2023-6.

Sharman, G.R., and Malkowski, M.A., 2020, Needles in a haystack: Detrital zircon U-Pb ages and the maximum depositional age of modern global sediment: Earth-Science Reviews, v. 203, p. 103-109, doi:10.1016/j.earscirev.2020.103109.

Sliwinski, J.T., Guillong, M., Liebske, C., Dunkl, I., Von Quadt, A., and Bachmann, O., 2017, Improved accuracy of LA-ICP-MS U-Pb ages of Cenozoic zircons by alpha dose correction: Chemical Geology, v. 472, p. 8–21, doi:10.1016/j.chemgeo.2017.09.014.

Solari, L.A., Ortega-Obregón, C., and Bernal, J.P., 2015b, U–Pb zircon geochronology by LAICPMS combined with thermal annealing: Achievements in precision and accuracy on dating standard and unknown samples: Chemical Geology, v. 414, p. 109–123, doi:10.1016/j.chemgeo.2015.09.008.

Suarez, C.A., Gonzalez, L.A., Ludvigson, G.A., Kirkland, J.I., Cifelli, R.L., and Kohn, M.J., 2014, Multi-Taxa Isotopic Investigation of Paleohydrology In the Lower Cretaceous Cedar Mountain Formation, Eastern Utah, U.S.A.: Deciphering Effects Of the Nevadaplano Plateau On Regional Climate: Journal of Sedimentary Research, v. 84, p. 975–987, doi:10.2110/jsr.2014.76.

Tolchard, F., Nesbitt, S.J., Desojo, J.B., Viglietti, P., Butler, R.J., and Choiniere, J.N., 2019, ‘Rauisuchian’ material from the lower Elliot Formation of South Africa and Lesotho: Implications for Late Triassic biogeography and biostratigraphy: Journal of African Earth Sciences, v. 160, doi:10.1016/j.jafrearsci.2019.103610.

Veevers, J.J., Cole, D.I., and Cowan, E.J., 1994, Permian-Triassic Pangean Basins and Foldbelts Along the Panthalassan Margin of Gondwanaland: Geological Society of America, Geological Society of America Memoirs, v. 184, doi:10.1130/MEM184.

Vermeesch, P., 2021, Maximum depositional age estimation revisited: Geoscience Frontiers, v. 12, p. 843–850, doi:10.1016/j.gsf.2020.08.008.

Viglietti, P.A. et al., 2021, Evidence from South Africa for a protracted end-Permian extinction on land: Proceedings of the National Academy of Sciences, v. 118, p. 1-21, doi:10.1073/pnas.2017045118.

Viglietti, P.A., Frei, D., Rubidge, B.S., and Smith, R.M.H., 2018, U-Pb detrital zircon dates and provenance data from the Beaufort Group (Karoo Supergroup) reflect sedimentary recycling and air-fall tuff deposition in the Permo-Triassic Karoo foreland basin: Journal of African Earth Sciences, v. 143, p. 59–66, doi:10.1016/j.jafrearsci.2017.11.006.

Von Quadt, A., Gallhofer, D., Guillong, M., Peytcheva, I., Waelle, M., and Sakata, S., 2014, U–Pb dating of CA/non-CA treated zircons obtained by LA-ICP-MS and CA-TIMS techniques: impact for their geological interpretation: J. Anal. At. Spectrom., v. 29, p. 1618–1629, doi:10.1039/C4JA00102H.

Walker, J.D., Geissman, J.W., Bowring, S.A., and Babcock, L.E., 2013, The Geological Society of America geologic time scale: Bulletin of the Geological Society of America, v. 125, p. 259–272, doi:10.1130/B30712.1.

Watts, K.E., Coble, M.A., Vazquez, J.A., Henry, C.D., Colgan, J.P., and John, D.A., 2016, Chemical abrasion-SIMS (CA-SIMS) U-Pb dating of zircon from the late Eocene Caetano caldera, Nevada: Chemical Geology, v. 439, p. 139–151, doi:10.1016/j.chemgeo.2016.06.013.

Widmann, P., Davies, J.H.F.L., and Schaltegger, U., 2019, Calibrating chemical abrasion: Its effects on zircon crystal structure, chemical composition and U Pb age: Chemical Geology, v. 511, p. 1–10, doi:10.1016/j.chemgeo.2019.02.026.

Wills, S., Choiniere, J.N., and Barrett, P.M., 2018, Predictive modelling of fossil-bearing locality distributions in the Elliot Formation (Upper Triassic–Lower Jurassic), South Africa, using a combined multivariate and spatial statistical analyses of present-day environmental data: Palaeogeography, Palaeoclimatology, Palaeoecology, v. 489, p. 186–197, doi:10.1016/j.palaeo.2017.10.009.

Yuguchi, T., Itoh, D., Yokoyama, T., Sakata, S., Suzuki, S., Ogita, Y., Yagi, K., Imura, T., Motai, S., and Ohno, T., 2023, Outlining zircon growth in a granitic pluton using 3D cathodoluminescence patterns, U Pb age, titanium concentration, and Th/U: Implications for the magma chamber process of Okueyama granite, Kyushu, Japan: Lithos, v. 440–441, p. 107026, doi:10.1016/j.lithos.2023.107026.

Žák, J., and Sláma, J., 2018, How far did the Cadomian ‘terranes’ travel from Gondwana during early Palaeozoic? A critical reappraisal based on detrital zircon geochronology: International Geology Review, v. 60, p. 319–338, doi:10.1080/00206814.2017.1334599.

Zi, J.W., Rasmussen, B., Muhling, J.R., and Fletcher, I.R., 2022, In situ U-Pb and geochemical evidence for ancient Pb-loss during hydrothermal alteration producing apparent young concordant zircon dates in older tuffs: Geochimica et Cosmochimica Acta, v. 320, p. 324–338, doi:10.1016/j.gca.2021.11.038.